

Allosteric Inhibition of the Tumor-Promoting Interaction between AIMP2-DX2 and HSP70

Dae Gyu Kim^{1,#}, Srigouri Huddar^{2,3,#}, Semi Lim¹, Jiwon Kong¹, Yuno Lee², Chul Min Park^{3,4}, Seungbeom Lee⁵, Young-Ger Suh^{5,6}, Minkyoung Kim⁷, Kyeong Lee⁷, Sunkyung Lee^{2,3,*}, and Sunghoon Kim^{1,*}

¹Medicinal Bioconvergence Research Center, Institute for Artificial Intelligence and Biomedical Research, College of Pharmacy & College of Medicine, Gangnam Severance Hospital, Yonsei University, Incheon 21983, Korea

²Drug Information research Center, Korea Research Institute of Chemical Technology, Daejeon 34114, Korea

³Korea University of Science and Technology, Daejeon 34114, Korea

⁴Center for Convergent Emerging Virus Infection, Korea Research Institute of Chemical Technology, Daejeon 34114, Korea

⁵College of Pharmacy, Cha University, Gyeonggi-do 11160, Korea

⁶College of Pharmacy, Seoul National University, Seoul 08826, Korea

⁷College of Pharmacy, Dongguk University, Goyang 10326, Korea

[#]These authors contributed equally to this work: Dae Gyu Kim and Srigouri Huddar

Running Title. Chemical inhibition of AIMP2-DX2-HSP70 interaction.

Corresponding Author.

Sunkyung Lee

Korea Research Institute of Chemical Technology, 141 Gajeong-ro, Yuseong, Daejeon
34114, Korea

Korea University of Science and Technology, 141 Gajeong-ro, Yuseong, Daejeon 34114,
Korea

OP +82-42-860-7148

Fax: +82-42-860-7096

Email: leesk@kriict.re.kr

Sunghoon Kim

Medicinal Bioconvergence Research Center, Department of Molecular Medicine and
Biopharmaceutical Sciences, Graduate School of Convergence Science and Technology,
College of Pharmacy, Seoul National University, Seoul, Korea.

Email: sungkim@biocon.snu.ac.kr

The number of Text pages: 36 pages

Number of Tables: 2

Number of figures: 7

Number of references: 37

Number of words in Abstract: 151 words

Number of words in Introduction: 539 words

Number of words in Discussion: 893 words

ABBREVIATIONS: AIMP, aminoacyl-tRNA synthetase-interacting multifunctional protein; AIMP2-DX2 (DX2), exon 2-depleted splice variant of aminoacyl-tRNA synthetase-interacting multifunctional protein 2; ARS, aminoacyl-tRNA synthetase; EV, empty vector; FBP, FUSE-binding protein; MMLV, Moloney murine leukemia virus; MSC,,: multi-tRNA synthetase complex; TGF β , transforming growth factor- β ; TNF- α , tumor necrosis factor- α ; TRAF2, TNF receptor-associated factor 2.

Section options. Drug discovery and Translational Medicine

ABSTRACT

Although protein-protein interactions (PPIs) have emerged as an attractive therapeutic target space, the identification of chemicals that effectively inhibit PPIs remains challenging. Here, we identified through library screening a chemical probe, compound **1** that can inhibit the tumor-promoting interaction between the oncogenic factor AIMP2-DX2 and HSP70. We found that compound **1** binds to the N-terminal subdomain of glutathione S transferase (GST-N) of AIMP2-DX2, causing a direct steric clash with HSP70 and an intramolecular interaction between the N-terminal flexible region (NFR) and the GST-N of AIMP2-DX2, which induces masking of the HSP70 binding region during molecular dynamics and mutation studies. Compound **1** thus interferes with the AIMP2-DX2 and HSP70 interaction and suppresses the growth of cancer cells that express high levels of AIMP2-DX2 *in vitro* and in preliminary *in vivo* experiment. This work provides an example showing that allosteric conformational changes induced by chemicals can be a way to control pathologic PPIs.

Significance Statement

Compound **1** is a promising protein-protein interaction inhibitor between AIMP2-DX2 and HSP70 for cancer therapy by the mechanism with allosteric modulation as well as competitive binding. It seems to induce allosteric conformational change of AIMP2-DX2 proteins and direct binding clash between AIMP2-DX2 and HSP70. The compound reduced the level of AIMP2-DX2 in ubiquitin-dependent manner via suppression of binding between AIMP2-DX2 and HSP70, and suppressed the growth of cancer cells highly expressing AIMP2-DX2 *in vitro* and in preliminary *in vivo* experiment.

INTRODUCTION

Since many physiological and pathological cellular events are controlled by protein-protein interactions (PPIs), modulating these PPIs promises attractive ways to develop drugs for many diseases (Nero et al., 2014; Ivanov et al., 2013). Although extensive efforts have been made to develop PPI inhibitors that target oncogenic interactions, most have failed due to a lack of structural understanding of the binding interface and limited efficacy using small molecules (Nero et al., 2014; Ran and Gestwicki, 2018; Li et al., 2018). Recently, a few meaningful advances in PPI inhibitor development have been reported using peptide mimetic molecules with molecular weights over 500 Da, but these molecules have shown limitations due to their molecular features including solubility, stability and cell penetration (Nero et al., 2014; Wójcik and Berlicki, 2016; Touti et al., 2019).

Aminoacyl-tRNA synthetase-interacting multifunctional protein 2 (AIMP2) functions as a scaffold for the assembly of the multisynthetase complex (MSC) (Kim, S. et al., 2011). AIMP2 dissociates from the MSC upon ultraviolet (UV) damage and transforming growth factor (TGF)- β , tumor necrosis factor (TNF)- α and Wnt signaling and functions as a tumor suppressor *via* its interaction with p53, FUSE-binding protein (FBP), Smurf2, TNF receptor-associated factor 2 (TRAF2) and dishevelled-1 (DVL1) (Han. et al., 2008; Kim et al., 2003; Kim, et al., 2016; Choi, et al., 2009; Yum et al., 2016). AIMP2-DX2 (hereafter referred to as DX2) is an alternative splicing variant of AIMP2 that lacks exon 2 and compromises the tumor suppressive activities of AIMP2 (Choi et al., 2011). DX2 is induced by carcinogens, and the level of DX2 is positively correlated with tumor aggressiveness and poor prognosis in lung, chemoresistant ovarian and colon cancers (Choi et al., 2011; Choi et al., 2012). Using the same protein structure to bind various signaling molecules, DX2 competitively interacts with the AIMP2-binding proteins p53, FBP and TRAF2, resulting in tumor-promoting

functions (Han et al., 2008; Kim et al., 2003; Kim et al., 2016; Choi et al., 2009). DX2 also independently shows oncogenic properties *via* a decrease in the level of p14 (Oh et al., 2016). Specific short hairpin RNAs (shRNAs) against DX2 and DX2-binding small molecules have been used in an attempt to reverse DX2-mediated tumor progression and have shown therapeutic effects *in vitro* and *in vivo* (Choi et al., 2011; Lee et al., 2013), suggesting DX2 as a novel therapeutic target against cancer. Recently, DX2 was shown to be stabilized by binding with heat shock protein 70 (HSP70), which blocks Siah1-mediated ubiquitination of DX2, and inhibition of the DX2/HSP70 interaction was found to be effective against DX2-induced tumor progression (Lim et al., 2019). Validation of DX2 and HSP70 as an effective cancer target encouraged us to establish a high-throughput screening method to identify chemicals that can specifically interfere with the interaction of these two oncogenic factors and elucidate effective hits with potentially different modes of action. Here, we investigated an allosteric inhibitor against the DX2 and HSP70 interaction to elucidate its mode of action on the suppression of tumors. We describe the studies on the selection and characterization, mode of action, and inhibition on cancer development of a chemical probe using binding assay, SPR (surface plasmon resonance), *in vitro* pull down assay, immunoprecipitation, cell viability assay, refolding assay, RT-PCR, xenograft, mutagenesis, and MD simulation.

Materials and Methods.

Chemistry. Commercially available reagents or solvents were used from freshly opened containers without further purification unless otherwise specified. Analytical thin-layer chromatography (TLC) analyses were conducted on precoated silica gel 60 GF254 plates. Purification of crude compounds was performed by flash chromatography on Merck silica gel

60 (230–400 mesh). ^1H NMR and ^{13}C NMR spectra were obtained on a Bruker 300 MHz NMR spectrometer at ambient temperature. Chemical shifts are given in ppm (δ) referenced to the internal standard tetramethylsilane (TMS). Coupling constants (J) are given in Hz. Mass spectra were obtained on a Bruker instrument by using electron impact techniques. Liquid chromatography/mass spectrometry (LC/MS) was employed to determine the purity of the compounds. LC/MS was carried out on a Waters ACQUITY Micromass (SQD2) equipped with a BEH C18 column (2.1 \times 50 mm, 1.7 μm) HPLC with a linear gradient of 10% to 90% acetonitrile into 0.2% $\text{CF}_3\text{CO}_2\text{H}/\text{H}_2\text{O}$ over 5 minutes at a flow rate of 0.4 mL/min. UV detection (photo diode array (PDA) detector (ACQUITY)) was carried out at a wavelength of 254 nm. High-resolution mass spectrometry (HRMS) analysis was performed using a UHR-TOF maXis 4G instrument (Bruker Daltonics, Bremen, Germany).

Ethyl (Z)-2-benzoyl-3-phenylacrylate (1), A mixture of benzaldehyde (6.24 mmol), ethyl 3-oxo-3-phenylpropanoate (5.20 mmol), benzoic acid (0.52 mmol), and piperidine (2.6 mmol) in toluene (30.0 mL) was heated at reflux under Dean-Stark conditions until the starting material disappeared by TLC analysis. After cooling to rt, the reaction mixture was concentrated under reduced pressure. The residue was purified by silica gel chromatography to afford ethyl (Z)-2-benzoyl-3-phenylacrylate **1** in 43% yield. ^1H NMR (300 MHz, CDCl_3) δ 8.0–7.95 (m, 3H), 7.62–7.55 (m, 1H), 7.49–7.42 (m, 2H), 7.41–7.36 (m, 2H), 7.31–7.26 (m, 3H), 4.25 (q, $J = 7.1$ Hz, 2H), 1.20 (t, $J = 7.1$ Hz, 3H). LC-MS ($\text{M}+\text{H}$) $^+$ 281.2. ^{13}C NMR: (75 MHz, CDCl_3) δ 195.67, 165.03, 142.62, 136.16, 133.92, 132.83, 131.32, 130.40, 130.21, 129.16, 128.85, 128.81, 61.58, 14.05. HRMS (EI^+) 280.1102.

Ethyl 3-(4-hydroxyphenyl)-3-oxopropanoate (12) (Miyatake-Ondozabal and Barrett, 2013). BBr_3 (1 M) in CH_2Cl_2 (8.9 mL, 8.9 mmol) was added with stirring to ethyl 3-(4-methoxyphenyl)-3-oxopropanoate (1 g, 4.49 mmol) in CH_2Cl_2 (30 mL) at -78°C . After

stirring for 1.5 h at -15°C, additional 1 M BBr₃ in CH₂Cl₂ (8.9 mL, 8.9 mmol) was added. After additional stirring for 2 h, MeOH (5 mL) and saturated aqueous NaHCO₃ were added to quench and neutralize the reaction to pH 7.0. The separated aqueous layer was extracted with CH₂Cl₂ (2 × 50 mL), and the combined organic layers were dried (MgSO₄), rotary evaporated and chromatographed (ethyl acetate (EtOAc):hexanes 3:7) to afford ethyl 3-(4-hydroxyphenyl)-3-oxopropanoate **12**. ¹H NMR (300 MHz, CDCl₃) δ 7.90 – 7.82 (m, 2H), 6.96 – 6.88 (m, 2H), 4.23 (q, *J* = 7.1 Hz, 2H), 3.99 (s, 2H), 1.27 (t, *J* = 7.1 Hz, 3H). LC-MS (M+H)⁺ 209.1.

Ethyl (Z)-2-(4-hydroxybenzoyl)-3-phenylacrylate (13) (Sun et al., 2009). The same reaction to prepare compound **1** was performed to provide **13** in 25% yield. ¹H NMR (300 MHz, CDCl₃) δ 7.94 (s, 1H), 7.91 – 7.83 (m, 2H), 7.39 – 7.34 (m, 2H), 7.27 – 7.22 (m, 2H), 6.87 – 6.83 (m, 2H), 4.24 (q, *J* = 7.1 Hz, 2H), 1.20 (t, *J* = 7.1 Hz, 3H). LC-MS (M+H)⁺ 297.2.

4-((Z)-2-(Ethoxycarbonyl)-3-phenylacryloyl)phenyl 5-((3a*S*,4*S*,6a*R*)-2-oxohexahydro-1*H*-thieno[3,4-*d*]imidazol-4-yl)pentanoate (15) (Ackerman et al., 2018). To a flame-dried round bottom flask, 5-((3a*S*,4*S*,6a*R*)-2-oxohexahydro-1*H*-thieno[3,4-*d*]imidazol-4-yl)pentanoic acid **14** (0.1 g, 0.409 mmol) and two drops of DMF were added to dry dichloromethane (2 mL). The mixture was cooled to 0°C, and oxalyl chloride (0.075 mL, 0.409 mmol) was added dropwise to the flask. The reaction was stirred for 3 h, after which a solution of ethyl (Z)-2-(4-hydroxybenzoyl)-3-phenylacrylate **13** (0.181 g, 0.613 mmol) and pyridine (0.050 mL, 0.613 mmol) in CH₂Cl₂ (2 mL) was added dropwise, and the reaction was allowed to stir overnight. When TLC showed completion of the reaction, the reaction mixture was diluted with water (10 mL) and washed with brine (2 × 15 mL). The organic layer was concentrated in *vacuo* and purified by automated column chromatography (eluting with EtOAc:hexanes 4:6) to afford product **15** (20 mg, 10% yield). ¹H NMR (300 MHz,

CDCl₃) δ 8.93 (d, $J = 0.9$ Hz, 1H), 8.02 – 7.96 (m, 3H), 7.36 (dd, $J = 7.9, 1.9$ Hz, 2H), 7.30 (dd, $J = 5.6, 1.3$ Hz, 1H), 7.28 – 7.23 (m, 1H), 7.21 – 7.15 (m, 2H), 6.90 (s, 1H), 4.86 (dd, $J = 7.5, 5.2$ Hz, 1H), 4.30 (dd, $J = 5.4, 2.8$ Hz, 1H), 4.24 (q, $J = 7.0$ Hz, 2H), 3.22 (dd, $J = 10.7, 5.1$ Hz, 2H), 2.98 (dd, $J = 13.6, 5.3$ Hz, 1H), 2.61 (t, $J = 7.3$ Hz, 2H), 1.87 – 1.71 (m, 5H), 1.58 (q, $J = 7.5$ Hz, 2H), 1.21 (t, $J = 7.1$ Hz, 3H). LC-MS (M+H)⁺ 523.2. ¹³C NMR: (101 MHz, CD₃OD) δ 194.67 (d, $J = 13.3$ Hz), 171.57, 164.95 (d, $J = 32.5$ Hz), 163.51, 155.45, 142.30, 141.50, 133.54, 133.00, 132.81, 131.74, 131.60, 131.13, 130.95, 130.51, 130.31, 130.09, 129.80, 128.55, 128.44, 127.86, 122.11, 115.30, 61.96, 61.51 – 60.73 (m), 60.23, 55.61, 39.66, 34.37 – 31.94 (m), 29.79 – 26.84 (m), 25.47 – 23.48 (m), 13.02 (d, $J = 2.4$ Hz). HRMS (FAB⁺) 523.1884.

Cell Culture and Materials. The CHO-K1 and A549 cell lines were purchased from the American Type Culture Collection (ATCC) and Korea Cell Line Bank, respectively. The H460, H358, H441, H1299, Calu-6, HCC-1588, H226, H1650, WI-26 and 293T cell lines were kindly gifted from Biocon (Medicinal Bioconvergence Research Center, Yonsei University). CHO, A549, H460, H358, H441, H1299, Calu-6, HCC-1588, H226 and H1650 cells were cultivated in RPMI medium supplemented with 10% fetal bovine serum (FBS) and 1% penicillin/streptomycin in 5% CO₂ at 37°C. 293T and WI-26 cells were cultured in DMEM under the same conditions as above. DX2 was cloned into the EcoRI/XhoI sites of the pcDNA3.0 and pEGFP-C2 vectors to express FLAG- and GFP-tagged DX2, respectively. Mutagenesis was performed with Quik-ChangeII (Promega) following the manufacturer's instructions. The purified human HSP70 (#ADI-NSP-555) protein was purchased from Enzo. The purified human tag-free DX2 proteins were kindly provided by the laboratory of Prof. Young Ho Jeon (Korea Univ.) MG-132 (#474790) and dox (#D3447) were purchased from Millipore and Sigma, respectively. Specific antibodies against DX2, AIMP2, KARS1,

MARS1, EPRS1 and AIMP1 were kindly provided by Biocon. The anti-Siah1 (#ab2237) antibody was purchased from Abcam, and specific antibodies against actin (#A1978) and FLAG (#F3165) were purchased from Sigma. Antibodies against HSP70 (#sc-24), ubiquitin (#sc-8017), CDK4 (#sc-23896) and GFP (#sc-9996) were purchased from Santa Cruz Biotechnology.

Molecular Modeling. For the relaxation of the protein (apo system) in the solvent system, we performed a 200 ns MD simulation using the DX2 structure consisting of residues L50-K251 without the disordered NFR. To examine the involvement of the NFR and binding mode of **1**, the NFR consisting of A38 to A49 was added into the protein structure in an inhibitor-bound state, followed by another 300 ns of simulation. The 300 ns simulation was repeated three times. The crystal structure of the AIMP2 GST domain (PDB ID: 5A34) (Cho et al., 2015). with a resolution of 2.6 Å was used for the molecular modeling study. The DX2 structure was constructed using the built and edited protein tools implemented in Discovery Studio (DS) 2018 software (<http://accelrys.com/products/collaborative-science/biovia-discovery-studio>). The binding site located in the GST-N was defined by CSP data obtained from NMR binding experiments (Lim et al., 2019). To generate initial docking poses subjected to the following MD simulation study, the docking simulation of compound **1** was performed using CDOCKER (Wu, G. et al., 2003). implemented in DS 2018 software. The MD simulations were performed using GROMACS 2016 with the Plumed plugin version 2.4 (Tribello et al., 2014). The Chamm36 all-atom force field was used for the protein and ligand and TIP3P was used for water. CHARMM-GUI (Jo, S. et al., 2008). was used for the generation of input for the simulations. The topologies and parameters of the ligands were generated by the CHARMM General Force Field (CGenFF) program (Vanommeslaeghe et al., 2010). A fully solvated cubic water box 10 Å thick was constructed for each system. The

systems were energy minimized by the steepest descent method to remove possible bad contacts until a tolerance of 1,000 kJ/mol. The constant particle number, volume and temperature (NVT) equilibration process was conducted for the minimized structures for 25 ps with a 1 fs time step at 303.15 K. The LINCS algorithm (Hess, B. et al., 1997). was used to constrain the bonds involving hydrogen atoms by their equilibrium bond lengths. Finally, the production runs were performed at a temperature of 303.15 K and a pressure of 1 bar by constant particle number, pressure and temperature (NPT) dynamics achieved with the Nosé–Hoover thermostat (Hoover, 1985) and Parrinello–Rahman (Parrinello and Rahman, 1981) barostat. The length of the time step was set to 2 fs for the production runs, and the trajectory was saved every picosecond. The cutoff values of short-range electrostatic interactions and van der Waals interactions were set to 12 Å. The particle particle-mesh Ewald method (Essmann et al., 1995). was used for long-range electrostatic interactions. To analyze protein–ligand interactions, the snapshot with the lowest nonbonded energy between the protein and ligand and a highly populated conformation of the ligand during the last 200 ns was selected as a representative structure. To avoid the ligand escaping from the binding site into the bulk solvent region, an upper-wall restraint force was applied to the system when the distance between the center of mass (COM) of the GST-N and the COM of **1** was greater than the cutoff limit (d_{up}) of 12 Å. For the wall, the harmonic potential was set with a force constant $\kappa=200$ kJ/mol·nm⁻².

$$\text{Bias}_{up} = \begin{cases} 0 & \text{for } d < d_{up} \\ k \cdot (d - d_{up})^2 & \text{for } d \geq d_{up} \end{cases}$$

The `g_mmpbsa` tool (Kumari et al., 2014) was used to calculate the binding energies of the system with MM-PBSA (molecular mechanics Poisson–Boltzmann surface area) method. The calculation was performed with 3,000 snapshots extracted from the 300 ns trajectory every 100 ps. We calculated the final binding free energy and the energetic contribution of

each residue by python scripts “MmPbSaStat.py” and “MmPbSaDecomp.py” which are the part of g_mmpbsa.

High Throughput Screening. DX2 and HSP70 were cloned into pBiT1.1-N[TK/LgBiT] and pBiT2.1-N[TK/SmBiT], respectively. LgBiT-PRKAR2A and SmBiT-PRKACA were obtained from Promega. CHO-K1 cells transfected with LgBiT-DX2 and SmBiT-HSP70 were seeded into 96-well white-bottom plates. After incubation for 24 h, the cells were treated with 6,186 chemicals (5 μ M each, KCB) in serum-free media for 4 h. Luciferase activity was detected using a NanoBiT assay system following the manufacturer’s protocol (Promega). Ninety-nine chemicals showing over 60% inhibition at 5 μ M were subjected to secondary screening using LgBiT-PRKAR2A and SmBiT-PRKACA for negative screening *via* the same experimental procedure as above. Ten compounds that showed no effect on the negative screening were subjected to a third screening involving *in vitro* pull-down assays and cell viability assays using DX2-inducible cell lines.

Surface plasmon resonance (SPR). To measure the binding affinity of **1** to the DX2 protein, we used a Reichert SR7500DC instrument (Reichert Technologies, Depew, NY). Thioredoxin (TRX)-tagged DX2 and TRX proteins were immobilized at levels of 11500 and 4000 RU, respectively, on a carboxymethyl dextran (CMDH) chip (Reichert, Depew, NY) with buffer containing 10 mM sodium acetate (pH 5.5). Compound **1** (1.5 - 50 μ M) in 2% dimethyl sulfoxide (DMSO)-containing PBS binding buffer (pH 7.4) flowed at a rate of 30 μ l/min. Sensorgrams were fitted to a simple 1:1 Langmuir interaction model ($A + B \rightleftharpoons AB$) using the Scrubber 2.0 analysis program (BioLogic Software, Australia, and Kaleida Graph Software, Australia) to calculate the values of K_a and K_D .

Fluorescence-Based Equilibrium Binding Assay. To determine the binding affinity of **1** to the DX2 protein, we performed fluorescence-based equilibrium binding experiments. All

titration experiments were conducted at 20°C using a Jasco FP 6500 spectrofluorometer (Easton, MD, USA). Purified human tag-free DX2 proteins were equilibrated with various concentrations of ligand **1** before fluorescence emission was measured. Ligand stock solutions were titrated into a protein sample dissolved in phosphate buffer (pH 7.4) containing 137 mM NaCl, 2.7 mM KCl, 10 mM Na₂HPO₄ and 2 mM KH₂PO₄. Protein samples were excited at 280 nm, and the decrease in fluorescence emission upon ligand binding was measured at 335 nm as a function of the ligand concentration. All titration data were fitted to a hyperbolic binding equation to obtain the K_D values.

Biomolecular Fluorescence Complement (BiFC) Assay. DX2 and HSP70 were cloned into the EcoRI/XhoI sites of the pCE-BiFC-VN173 and pCE-BiFC-VC155 vectors to tag Venus-N173 and Venus-C155, respectively. CHO cells expressing VN173-DX2 and VC155-HSP70 were treated with **1** in a dose-dependent manner for 4 h. After incubation, the cells were washed with cold PBS three times and fixed with 100% cold methanol for 10 minutes, and the nuclei were stained with DAPI for cell counting. The BiFC signal was determined by confocal microscopy, and signal-positive cells were counted in the same number of cells. The experiment was independently repeated three times.

In vitro Pull-Down Assay. DX2 was cloned into the EcoRI/XhoI sites of the pGEX4T-1 vector to express GST-tagged DX2. The purified GST or GST-DX2 proteins were mixed with the HSP70 protein (#ADI-NSP-555, Enzo) in 50 mM Tris-HCl (pH 7.4) buffer containing 100 mM NaCl, 0.5% Triton X-100, 10% glycerol, 1 mM EDTA, and protease inhibitor (Calbiochem), followed by treatment with **1** or not for 4 h. After incubation, proteins coprecipitated with beads were washed three times with incubation buffer excluding 0.5% Triton X-100, subjected to SDS-PAGE, and detected by Coomassie staining. To examine the binding of **1** to the DX2 or HSP70 proteins, we incubated **15** with 100 µg of tag-free DX2 or

HSP70 proteins as starting amounts for 12 h in incubation buffer and performed the same procedure described above. Biotin alone was used as a negative control compound for **15**.

Immunoprecipitation. The cells were lysed with 50 mM Tris-HCl (pH 7.4) lysis buffer containing 100 mM NaCl, 0.5% Triton X-100, 0.1% SDS, 10% glycerol, 1 mM EDTA, and protease inhibitor (Calbiochem). Two hundred micrograms of total cell lysates as starting amounts were mixed with specific antibodies and preincubated with agarose beads for 12 h against the proteins of interest. After mixing, proteins coprecipitated with agarose beads were gently washed with cold lysis buffer excluding 0.5% Triton X-100 and 0.1% SDS three times and separated by SDS-PAGE. Proteins were detected by immunoblotting using specific antibodies against the proteins of interest. To determine the **1**-mediated ubiquitination of DX2, the cells were treated with **1** and MG-132 (50 μ M) for 12 h. The cells were then lysed with 50 mM Tris-HCl (pH 7.4) buffer containing 100 mM NaCl, 0.5% Triton X-100, 1% SDS, 10% glycerol, 1 mM EDTA, protease inhibitor (Calbiochem) and the pan-deubiquitinase inhibitor PR-619 (Sigma-Aldrich), boiled at 100°C for 10 minutes, and then diluted in lysis buffer including 0.1% SDS (Crespo-Yañez et al., 2018). The following experimental procedures were performed as described above.

Xenograft. H460 cells (1×10^7) were subcutaneously injected into the left and right sites of the backs of 7-week-old female BALB/cSLC-*nu/nu* mice (Central Lab Animal Inc., Korea). Five or 10 mg/kg **1** was intraperitoneally administered to the mice (n=3/group) every other day for 10 days. The volumes of the embedded tumors and body weights were measured five times over the experimental period. After 10 days, all mice were sacrificed, and the embedded tumors were excised. The weights of the harvested tumors were measured, and photos of the whole-body embedded tumors and excised tumors were taken. To determine the level of the DX2 protein in the embedded tumors, the excised tumors were homogenized and

lysed in PBS containing 1% Triton X-100, 0.1% SDS and protease inhibitor (Calbiochem). Supernatants after centrifugation at 15000 rpm at 4°C for 30 minutes were subjected to SDS-PAGE and immunoblotting using a specific antibody against DX2. Animal experiments were approved and performed in compliance with the University Animal Care and Use Committee guidelines at Yonsei University.

3D Culture. H460 cells in 2D culture conditions were detached from the culture plate using Accumax (EMD Millipore). After cell counting using the disposable hemocytometer C-Chip (INCYTO), we diluted the cells to a concentration of 5,000 cells/100 μ l in medium supplemented with 10% FBS and 1% penicillin/streptomycin. The cells were then seeded onto ultralow attachment 96-well 3D culture plates (Corning). After incubation for 48 h, the spheroids and cancer cells cultivated under 3D culture conditions were treated with **1** for 72 h, and cell viability was determined using a CellTiter-Glo 3D cell viability assay (Promega) following the manufacturer's instructions. The experiment was independently repeated three times.

Anchorage-Independent Colony Formation Assay. To generate stable cells, we introduced FLAG-tagged DX2 WT and mutants into A549 or H460 cells for cultivation in medium containing G418 (800 μ g/mL, #G0175, Duchefa) for the selection of cells stably expressing the ectopically introduced plasmids. After culture for two weeks, the settled colonies were selected, and the level of overexpressed DX2 was determined by immunoblotting using an anti-FLAG antibody. Each of the stable cells was subjected to an anchorage-independent colony formation assay using a cell transformation assay kit (Cell Biolabs, Inc.) following the manufacturer's instructions. The number of colonies stained by hematoxylin (Sigma) was counted. The experiment was independently repeated three times.

Cell Viability Assay. DX2-inducible or empty vector (EV)-inducible A549 isogenic cells (2×10^3 cells/well) were cultured in 96-well flat bottom plates and pretreated with dox (Sigma) to induce DX2 expression. After pretreatment with dox for 24 h, the cells were cultured in serum-free medium diluted with chemicals for 48 h. To check the resistance vulnerability, H460 cells pretreated with **1** (0.5 μ M) for three weeks were treated with chemical in a dose-dependent manner for 72 h. MTT solution (5 mg/mL, Sigma) was added to each well followed by incubation for 1.5 h. After the medium was discarded, the precipitated formazan crystals were solubilized with DMSO (Duchefa), and the absorbance was measured at 560 nm using a microplate reader (Sunrise, Tecan). All of the experiments were repeated three times independently.

Refolding Assay. Using a Protein Refolding Kit (Boston Biochem) following the manufacturer's instructions, the effects of the compound on the protein refolding process was examined. Purified proteins HSP70 and HSP40 and Glow-Fold Substrate were mixed with **1** in reaction buffer containing Mg^{2+} ATP, and all of the reagents were incubated for 5 minutes at room temperature. To unfold the substrate, the mixture was heated at 50°C for 8 minutes and left on ice for 10 minutes. The refolding reaction was conducted at 30°C for 1.5 h, and the luminescence signal from the refolded substrate was measured with a plate reader (Glomax, Promega). Experiments were independently repeated three times.

RT-PCR. Total RNA extracted from H460 cells using the RNeasy Mini Kit (Qiagen) was used for RT-PCR with dNTPs, random hexamers and Moloney murine leukemia virus (MMLV). To determine the mRNA expression of DX2, AIMP2 and actin, we used 2 μ l of cDNA in the PCR with the following specific primers. DX2: CTGGCCACGTGCAGGATTACGGGG and AAGTGAATCCCAGCTGATAG; AIMP2: ATGCCGATGTACCAGGTAAAG and CTTAAGGAGCTTGAGGGCCGT; actin:

CCTTCCTGGGCATGGAGTCCT and GGAGCAATGATCTTGATCTT. Actin was used as a loading control.

Statistics.

Statistical tests were performed with Prism (GraphPad). A value of $P < 0.05$ was considered statistically significant. All error bars represent standard deviation (S.D.). For quantitative data, statistical parameters are reported in the figure legends.

RESULTS

Selection and characterization of a chemical probe. Our previous report demonstrated that DX2 is stabilized by its interaction with HSP70 and that inhibition of the interaction between these two proteins reduces DX2-mediated cancer proliferation (Lim et al., 2019). Therefore, we searched for an inhibitor of this interaction to suppress DX2-dependent cancer progression using a luciferase-based complementation assay system (Dixon et al., 2016), established for high-throughput screening (Figure 1a). In a primary screening using 6,186 compounds from the Korea Chemical Bank (KCB), 99 compounds showed over 60% inhibition at 5 μM (Figure 1b, upper and Supplemental Figure S1a). The specificity of these 99 compounds for DX2 was determined using the binding pair protein kinase A catalytic subunit (PRKACA) and protein kinase A type 2A regulatory subunit (PRKAR2A) (Dixon et al., 2016) and 10 compounds were found to specifically suppress the binding between DX2 and HSP70 but not PRKACA-PRKAR2A (Figure 1b and c). Further validation of the 10 compounds was carried out using *in vitro* pull-down and cell viability assays. An *in vitro* pull-down assay using the purified HSP70 and glutathione S-transferase (GST)-DX2 proteins demonstrated that compound **1** significantly inhibited the interaction of these two proteins (Figure 1d). Furthermore, **1** suppressed DX2-dependent cell proliferation in a DX2-inducible

system (Figure 1e and b bottom). Using this three-step screening procedure, we identified compound **1** as a potential PPI inhibitor of DX2 and HSP70 (Figure 1f).

Additionally, the usefulness of compound **1** as a starting point for the optimization of the discovery of an anticancer agent was validated through the examination of preliminary structure-activity relationships (SARs) on a series of 8 compounds in KCB libraries (Table 1). There were 8 compounds (**2** ~ **9**) with ene-dione moieties in the KCB whose biological activities on DX2 were evaluated at 5 μ M. Compounds **2** ~ **4** substituted at the 3 or 4 positions of the R¹ benzene ring showed 66%, 76%, and 53% inhibition, respectively. Replacement of the ester at R² with amide **5** (56% inhibition), arylketo **8** (58% inhibition), and alkylketo **9** (58%) retained the compound's ability to inhibit the interaction between DX2 and HSP70. Additionally, the introduction of biaryl groups (**8**, **9**) at R³ was tolerable for activity and a variety of variations at R³ might be possible. Additionally, **1** can form a covalent bond with DX2 by a nucleophilic addition. Then, we examined compounds **10** and **11** without the site required for nucleophilic addition among the KCB libraries, resulting in retention of the inhibitory activities (Table 2). Based on this preliminary SAR study, we synthesized compound **1** and its biotinylated derivative **15** by conventional procedures (Miyatake-Ondozabal and Barrett, 2013; Sun et al., 2009; Ackerman, 2018). (Figure 2) for biological evaluation, including dose dependency, functional assays in cell lines, and studies on the mode of action. Because compound **4** with a (4-phenylpropoxy)benzyl group at R¹ was active (53% inhibition) in the screening, we primarily attempted to prepare **15**, where the 4-position of the benzene ring at R¹ is biotinylated. Fortunately, compound **15** showed similar activity to **1** and was used to study the mode of action (Supplemental Figure S3a and b). In summary, compounds with 3 or 4 substituents on the benzoyl moiety retained activity, and the introduction of a biaryl group at C3 instead of a benzene group was tolerable for efficacy. The

replacement of the ester group with a more metabolically stable keto or amide group also maintained activity, suggesting that the structure of **1** can be broadly modified to improve efficacy and safety and should be useful as a chemical probe to elucidate the mode of action on DX2.

We examined the inhibitory activity of compound **1** for further validation as a chemical probe (Figure 3). The IC_{50} value of **1** was determined to be 2.9 μ M for inhibiting the binding between DX2 and HSP70, but the IC_{50} was over 100 μ M for the inhibition of PRKACA and PRKAR2A binding (Figure 3a), indicating that **1** specifically interrupted the binding between DX2 and HSP70. Next, time-dependent binding inhibition of **1** was also confirmed (Supplemental Figure S2a). Compound **1** did not show time-dependent inhibitory activity on the binding between DX2 and HSP70, which indirectly indicates that inhibition of DX2 by **1** is not based on covalent modification. To exclude the possibility of artifacts of our screening system, we determined the effects of **1** in a complementary fluorescence-based assay, and the same result was observed (Supplemental Figure S2b). The endogenous interaction of the two proteins was found to be abrogated by treatment with **1** by reciprocal immunoprecipitation, implying its physiological function (Figure 3b). We also examined whether **1** suppresses the direct binding of these two proteins in a dose-dependent manner *via* a pull-down assay; similar to the other assays, we observed dose-dependent inhibition of their direct binding (Figure 3c). Additionally, we tested whether depletion of **1** induces the binding of DX2 and HSP70. The compound **1**-mediated decrease in the binding of the two proteins was recovered by adding fresh medium (Figure 3d), indicating that **1** inhibits the binding of the two proteins. Together, these observations indicate that **1** specifically interferes with the binding of DX2 with HSP70.

Because inhibition of the interaction between DX2 and HSP70 has been reported to lead to the turnover of DX2 *via* ubiquitination (Lim et al., 2019), we examined whether **1** destabilizes the DX2 protein. First, we monitored the protein and mRNA levels of DX2 upon treatment with different doses of **1** and found that **1** specifically reduced the DX2 protein level but not the mRNA level (Figure 3e). We also observed increased ubiquitination of DX2 upon treatment with **1**, which was found to be mediated by its increased binding to Siah1, an E3 ligase against DX2 (Lim et al., 2019), and decreased binding to HSP70 (Figure 3f), implying that **1** induces the binding of Siah1 to DX2 by interfering with HSP70 access, resulting in DX2 turnover. The significance of Siah1 on compound **1**-mediated degradation of DX2 was also investigated by knockdown of Siah1 *via* its specific siRNA. When Siah1 was knocked down, the level of DX2 basically increased without HSP70 expression, and there was no decrease in DX2 despite treatment with **1** (Figure 3g), suggesting that Siah1 is critical for the compound **1**-dependent decrease in DX2. We further validated that **1** did not affect the protein level of AIMP2 or other aminoacyl-tRNA synthetases (ARSs), which are AIMP2-interacting proteins in the MSC (Kim et al., 2011). (Figure 3e and Supplemental Figure S2c, upper). We also determined the level of CDK4, a known downstream molecule of HSP70 (Lim et al., 2019), and the protein-folding activity of HSP70 upon treatment of **1** to elucidate the possibility that **1** could inhibit the interaction of DX2 and HSP70 based on the interaction with HSP70. We confirmed that there was no effect on the level of CDK4 or on the folding activity of HSP70 (Supplemental Figure S2c, bottom and 2d), suggesting the PPI inhibition based on the interaction with DX2, not on the interaction with HSP70 of **1**. Altogether, these data led to the conclusion that compound **1** inhibited the interaction between DX2 and HSP70, resulting in DX2 degradation *via* recruitment of Siah1.

Mode of action study of compound 1. To unveil the mode of action of compound **1**, we utilized biotin-conjugated compound **15**. First, we compared the function of **15** with that of the original compound **1**. Treatment of H460 cells with **15**, similar to **1**, reduced the binding of HSP70 to DX2 and destabilized the DX2 protein (Supplemental Figure S3a and b), suggesting that the conjugated biotin compound retained its function. We then examined whether **15** bound directly to DX2 or HSP70 using an *in vitro* pull-down assay and observed direct binding between the compound and DX2, not HSP70 (Figure 4a). We further performed a competitive binding assay using **15** and **1** to determine the specific binding of the chemical to DX2 or HSP70. The DX2 protein, not HSP70, was pulled down by **15**, and the amount of coprecipitated DX2 was reduced by the addition of **1**, implying the specific binding of **1** to DX2 and not HSP70 (Figure 4b). We also confirmed the competitive binding of **1** and **15** to endogenous DX2 proteins as above *via* the treatment of H460 cells with the two compounds (Figure 4c). Next, we measured the binding affinity of **1** to DX2 *via* a surface plasmon resonance (SPR) assay and determined a K_D value of 12 μM (Figure 4d), which was similar to the IC_{50} value obtained for the inhibition of the interaction between DX2 and HSP70 (Figure 3a), implying the significance of the binding of the compound to DX2 for inhibition of the DX2-HSP70 interaction. We further confirmed the binding affinity *via* a fluorescence-based equilibrium binding experiment (Breen et al., 2016) and obtained a binding affinity similar to that stated above (Supplemental Figure S3c). The results from two other binding assays suggested that direct binding of **1** to DX2 could affect protein function. We also determined which domain of DX2 bound to **1**. DX2 was divided into the N-terminal flexible region (NFR), GST domain (GST), and C-terminus of the GST domain (GST-C) (Lim, S. et al., 2019). (Figure 4e, right), and each fragment was mixed with **1**. The *in vitro* pull-down assay using streptavidin-Sepharose beads revealed that the NFR and GST-N, a

region known for binding with HSP70 (Lim et al., 2019), were bound by **1** (Figure 4e, left), further validating **1** as a PPI inhibitor. All of the binding data imply that **1** inhibits the interaction between DX2 and HSP70 *via* direct binding with DX2.

To investigate the binding mode of compound **1** with DX2, we performed a molecular modeling study because the disordered NFR was not visible in other structural assays (Lim et al., 2019). Due to the disordered nature of the NFR, the replicated run of 300 ns molecular dynamics (MD) simulations were conducted three times. The initial pose of **1** for MD simulation with the highest docking score of 34.94 was obtained from molecular docking simulation using CDOCKER. To increase the chance of determining the binding event and to properly adjust the position of **1** to fit into the GST-N, we performed MD simulations with the upper-wall restraint force. Because ligand binding is a rare event in the simulation considering the protein flexibility in the solvent system, this binding event was observed in only one trajectory among three replicated systems with the upper wall. From this trajectory, we found that **1** sought the proper hydrophobic fit into the GST-N for the beginning 100 ns (Figure 5a). The DX2 was well stabilized at around 0.45 nm of C α -RMSD (Supplemental Figure S4a). While the C α -RMSD values are relatively fluctuating during beginning 200 ns, the binding conformation of **1** was well maintained in the GST-N for the last 200 ns, showing stable interactions with three significant residues, Y47, N56 and K129 (Figure 5b). C α -RMSF on DX2 represented the significant conformational change of the N-terminal region during beginning 200 ns simulation time. Not only the most residues in binding region but also the N-terminal region which is generally fluctuating, seemed to be very stable during the last 100 ns (Supplemental Figure S4b). The snapshot at 211.3 ns, having the lowest nonbonded energy (Supplemental Figure S4c) between DX2 and a highly populated conformer of **1** during the last 200 ns (Inset of Supplemental Figure S4a), was selected as a representative structure for

further interaction analysis. For the energetics of the binding mode between **1** and DX2, we calculated the total binding energy using MM-PBSA method. The binding structure was stabilized from initial -21.33 kJ/mol to averaged -37.21 ± 13.08 kJ/mol of total binding energy over the last 100 ns (Supplemental Figure S4c). The energy of representative structure at 211.3 ns was -46.31 kJ/mol. To validate the important amino acids in the protein-ligand interaction, per-residue energy decomposition analysis was performed with the 300 ns simulation trajectory. From this analysis, we found that the three key residues (Tyr47, Asn56, and Lys129) are located at the lowest nonbonded interaction energies (Supplemental Figure S4d), which is well correlated with the mutation analysis. The carbonyl groups of the benzoyl and ester moieties on **1** interact with the side chains amines of N56 and K129, respectively, by H-bonding (Supplemental Figure S4b). There was a π - π interaction between the styrene of **1** with Y47 of DX2. To validate the MD simulation results, we generated alanine mutants of the DX2 amino acids that were suggested to be critical for the binding of **1**. First, we examined the binding of the alanine mutants to the chemicals using **15** via an *in vitro* pull-down assay. Wild-type DX2 (DX2 WT) and most of the mutants tested showed strong binding, but the binding of the DX2 mutants Y47A, N56A and K129A to **15** was significantly reduced (Figure 5c). Next, we determined whether **1** diminished the binding between HSP70 and DX2. Based on the immunoprecipitation results using the expressed mutants in 293T cells, we determined that **1** abrogated the interaction between HSP70 and DX2 WT but not Y47A, N56A or K129A, as described above (Figure 5d). Because Y47, N56 and K129 are critical residues of DX2 for binding with **1**, we tested the **1**-mediated ubiquitination of the selected DX2 mutants. From the ubiquitination assay, we observed that DX2 WT was ubiquitinated upon treatment with **1**, resulting in a decreased level of DX2, but DX2 ubiquitination and DX2 protein expression of the tested mutants were not affected by

treatment with **1** (Figure 5e). Together, these observations indicate that the pocket surrounded by Y47, N56 and K129 in the NFR and GST-N of DX2 is critical for binding with **1**.

The NFR was shown to be involved in the binding of compound **1** to the GST-N of DX2 (Figure 6 and Supplemental Movies S1 and S2). Among the three significant interacting residues, Y47 is located in the NFR and has a stable hydrophobic interaction with **1**. Moreover, a stable hydrophobic interaction between L50 and T117 was shown in the chemically bound system but not in the apo system (Figure 6a), indicating that the disordered NFR containing L50 has no chance to interact with the GST-N containing T117 without **1** binding. Interestingly, along with being involved in the binding of **1**, the NFR binds with the surface of DX2 through intramolecular hydrophobic interactions, meaning that the binding of the NFR to GST-N could mask the L97 and T117 residues, which are significant residues for the binding to HSP70 (Lim et al., 2019).. In particular, hydrophobic interactions of G40, Y47 and L50 in the NFR with L97 and T117 on the surface of GST-N were observed in the representative structure of the system (Figure 6b). The induced binding of the NFR and GST-N in the presence of **1** seemed to significantly increase the area of the bumping region to interfere with the interaction between DX2 and HSP70 (Figure 6c). These analyses revealed that the interaction of **1** in the pocket of DX2 surrounding Y47, N56 and K129 induces a steric clash against HSP70 by direct binding interference and a conformational change in DX2, resulting in turnover of the DX2 protein.

Inhibition of cancer development via compound 1. Because compound **1** leads to the degradation of DX2 *via* inhibition of binding with HSP70, we examined whether **1** suppresses cancer cell proliferation. H460 cells showing a high level of DX2 were treated with **1**, and cell viability was shown to decline in a dose-dependent manner (Figure 7a, red circle). We further determined whether **1**-mediated suppression of cell viability was

dependent on the level of DX2. After examining the levels of DX2 and HSP70 in various lung cells (Supplemental Figure S5a), the cells were subjected to a cell viability assay upon treatment with **1**, and the 50% inhibition concentration (EC_{50}) of cell proliferation was calculated. The cells with the highest levels of DX₂, H460 and H358, showed the lowest EC_{50} values among the tested cell lines (Figure 7a, red), and the EC_{50} values were very similar to the IC_{50} and K_D previously determined for the inhibition of binding between DX2-HSP70, implying that suppression of the interaction between DX2 and HSP70 using **1** leads to cell death. Normal (WI-26) and cancerous (H1650) lung cells, those with the lowest level of DX2, were not affected by **1** (Figure 7a, yellow), further suggesting that DX2 is required for **1** to affect cell death. The significance of the DX2 level on **1**-mediated suppression of cell proliferation was also determined in DX2-knockdown H460 and H358 cells by introducing specific siRNA (Supplemental Figure S5b). A time-dependent inhibitory effect of cancer cell proliferation *via* **1** was also confirmed (Supplemental Figure S5c). Before determining the *in vivo* efficacy of this compound, we treated H460 cells with **1** in a 3D cell culture system. Compound **1** dose-dependently decreased the proliferation of H460 spheroids in the 3D environment (Figure 7b), implying that **1** could function in an *in vivo* model. The IC_{50} of **1** in 3D culture was much higher than that in 2D system, which might be due to the poor penetration of compound into the spheroids as mentioned in publications (Park, M. C. et al., 2016; Langhans, S. A., 2018). We further validated the effects of **1** on cancer cell progression *in vivo* via a xenograft model using H460 cells. Compound **1** was intraperitoneally injected at doses of 5 and 10 mg/kg, and tumor growth and body weight were monitored over the experimental periods. Even though it is preliminary data due to small number of mice per each group, administration of **1** significantly reduced tumor size in a dose-dependent manner with little effect on body weight (Figure 7c, left and Supplementary Figure S5d). A reduction

in tumor weight was also observed (Figure 7c, middle). We further validated the endogenous levels of the DX2 and HSP70 proteins in the excised tumors from the mice. The level of DX2, but not HSP70, was found to be decreased after injection of **1**, and the quantified level is shown as a graph excluding the confusion from object variation (Supplemental Figure S5e), implying that treatment with **1** led to inhibition of cancer proliferation *via* degradation of the DX2 protein.

To unveil the dependency of the effects of **1** on its binding with DX2, we generated A549 cell lines stably expressing DX2 WT or binding-defective mutants Y47A, N56A and K129A and treated these cells with various doses of **1**. The EC₅₀ value of these A549 stable cells expressing DX2 WT (0.92 μM) was very similar to the EC₅₀ found in H460 cells (0.97 μM) (Figure 7d, red, 7a), emphasizing the significance of the DX2 level on the function of **1**. However, there was no effect from **1** in cell lines expressing DX2-binding-defective mutants (Figure 7d, blue), suggesting that the decreased cell viability induced by treatment with **1** is mediated by its binding with DX2. We further examined the significance of the binding of **1** to DX2 *via* an anchorage-independent colony-forming assay. As expected, the number of colonies and the efficacy of **1** both increased in cells stably expressing DX2 WT but not in the mutant cell lines (Figure 7e). The above two assays showed that abrogation of the binding between DX2 and **1** prevented the chemical-mediated inhibition of cancer cell development, leading us to the conclusion that the binding of **1** to DX2 is critical for the function of **1**. To examine the resistance vulnerability of **1**, we determined the EC₅₀ of **1** in H460 cells pretreated with chemicals for three weeks and compared it with that of native H460 cells. A small decrease in EC₅₀ was observed, but **1** efficiently decreased cell viability even though it was used as a pretreatment (Supplemental Figure S5f), meaning that compound **1** could also function for a long time.

DISCUSSION

DX2 is considered a novel target for cancer therapeutics because of its oncogenicity, and specific siRNA and small molecules targeting DX2 have been studied as therapeutic strategies for DX2-expressing tumors (Choi et al., 2011; Lee et al., 2013). Despite many trials, none of the examined tools have been shown to efficiently target DX2. Recently, HSP70 was shown to significantly affect the protein level of DX2 by blocking the access of Siah1, a specific E3 ligase, leading to the suggestion that a PPI inhibitor between DX2 and HSP70 may be a good tool to target DX2 (Lim et al., 2019). Here, we suggest compound **1** as a novel PPI inhibitor for the binding of DX2 and HSP70 and fully address the functional mode of action of this compound. We identified **1** as a hit compound for a PPI inhibitor targeting the interaction of DX2 and HSP70 using a luciferase-based complementation system (NanoBiT) (Lim et al., 2019). Compound **1** has the possibility of forming a covalent bond with DX2 by nucleophilic addition. Then, we examined compounds **13** and **14** without the site for nucleophilic addition, resulting in retention of the inhibitory activity (Table 2). Additionally, **1** did not show time-dependent inhibitory activity on the binding of DX2 and HSP70 (Supplemental Figure S2a). These results indirectly indicate that inhibition of DX2 by **1** is not based on covalent modification. Compound **1** was found to inhibit and induce the binding of HSP70 and Siah1 to DX2, respectively, resulting in ubiquitination-dependent degradation of DX2. Furthermore, **1** was shown to reduce cancer cell development *in vitro* and in preliminary *in vivo* experiment in a DX2-dependent manner. We further analyzed the mode of action of **1**. The binding of **1** to DX2 is important for DX2 cellular function, and DX2 residues Y47, N56 and K129 appeared to be significant for binding *via* MD simulation and mutational analysis. Two modes of action of **1** were proposed: allosteric modulation of the DX2 structural conformation and direct steric clashing of DX2-HSP70 binding.

Because a structural understanding of target proteins is critical for drug discovery, many target proteins have been analyzed using techniques such as X-ray crystallography and nuclear magnetic resonance (NMR) analysis. However, assessing the structure of the full-length protein *via* the above traditional analyses is difficult because many proteins have an unstructured flexible region. This flexible region has been reported to be significant for protein function (Babu, 2016); therefore, there have been many efforts to overcome this limitation. DX2 has a disordered NFR consisting of 50 amino acids. To determine whether the mode of action of **1** was associated with the NFR, we conducted MD simulations. The MD simulations suggested that compound **1** binds the pocket surrounding the NFR (Y47) and GST-N (N56 and K129), which was indirectly confirmed *via* mutagenesis experiments. Through the MD study, we also unveiled the mode of action of **1**, which directly interferes with access to HSP70 and masks the HSP70 binding surface of DX2 *via* a hydrophobic interaction between the NFR and the GST-N binding site in the bound state of **1**. From these results, we demonstrated that the NFR and GST-N might be critical for the binding of DX2 to HSP70, further supporting the described mode of action of **1**. Although some DX2 exists in its free form, the possibility that DX2 could be constitutively bound to HSP70 still exists. Therefore, structural analysis with **1** *via* MD simulations needs to be considered with HSP70 bound to DX2 for competitive binding, and this will be our further study.

Many of the 650,000 PPIs estimated from proteomics tools have recently been reported to be oncogenic (Ran and Gestwicki, 2018; Li et al., 2018). Therefore, PPIs have been considered to be a significant therapeutic target, especially for cancer, and many trials have sought to discover PPI inhibitors that interfere with oncogenic PPIs (Nero et al., 2014; Ivanov et al., 2013). The discovery of small molecule PPI inhibitors is now a research focus because of the importance of PPIs in cancer. Here, we identified **1**, with a molecular weight of less than 500

Da, as a PPI inhibitor that efficiently suppresses the oncogenic binding between DX2 and HSP70. Our results showing PPI inhibition using a small molecule with a molecular weight of less than 500 Da could provide new encouragement to continue the search for the discovery of PPI inhibitors using small molecules, which exhibit fewer problems in the clinical setting than large molecules. Cancer patients suffer from the side effects of therapeutic agents against cancer. Treatment with **1** did not affect normal cell proliferation (Supplementary, Table S1) or the body weights of the tested mice, suggesting that **1** has no or only small side effects. This advantage may be due to the PPI inhibition mode of action; specific inhibition of the interaction between DX2 and HSP70 led cancer cell regression without affecting normal cells. We also evaluated metabolic stability of compound **1**. The remaining amount of compound **1** was determined using LC-MS/MS analysis (Mass spectroscopy: Agilent6460, HPLC: Agilent1261) upon incubation with rat and human liver microsomes for 30 min, which provided 8.76% and 7.02%, respectively (Supplemental, Table S2). The metabolic stability of compound **1** is very poor, and further optimization is needed to improve its physicochemical properties as well efficacy for the discovery of a sustainable lead on antitumor agent based on the inhibition of DX2 and HSP70 interaction.

CONCLUSION

We identified compound **1** to inhibit the tumor-promoting protein-protein interaction between AIMP2-DX2 and HSP70 through allosteric modulation as well as competitive binding. We performed MD simulations, mutagenesis analyses and characterization of biological function using compound **1** and its biotin-conjugated chemical **15** to elucidate the mode of action of compound **1**. Compound **1** seems to induce allosteric conformational changes in the AIMP2-DX2 protein and direct binding clashes between AIMP2-DX2 and HSP70. Compound **1** reduced the AIMP2-DX2 protein level in a ubiquitin-dependent manner via suppression of

the binding between AIMP2-DX2 and HSP70 and suppressed the growth of cancer cells highly expressing AIMP2-DX2 *in vitro* and in preliminary *in vivo* experiment. This paper presents a novel chemical route to interfere with oncogenic PPIs.

Authorship Contributions

Participated in research design: Kim D, Huddar, Lim, Lee Y, Park, Lee K, Lee Su, Kim S

Conducted experiments: Kim D, Huddar, Lim, Kong, Park, Lee Se, Kim M

Contributed new reagents or analytical tools: Kim D, Lim, Park

Performed data analysis: Kim D, Huddar, Lee Y, Park, Suh, Lee K, Lee Su, Kim, S

Wrote or contributed to the writing of the manuscript: Kim D, Huddar, Lee Y, Park, Lee Su, Kim S

References

- Ackerman LKG, Martinez Alvarado JI, Doyle, AG (2018) Direct C–C Bond Formation from Alkanes Using Ni-Photoredox Catalysis. *J. Am. Chem. Soc* **140**: 14059-14063.
- Babu, MM (2016) The Contribution of Intrinsically Disordered Regions to Protein Function, Cellular Complexity, and Human Disease. *Biochem. Soc. Trans* **44**: 1185-1200.
- Breen CJ, Raverdeau M, Voorheis, HP (2016) Development of a Quantitative Fluorescence-Based Ligand-Binding Assay. *Sci. Rep* **6**: 25769.
- Cho HY, Maeng SJ, Cho HJ, Choi YS, Chung JM, Lee S, Kim HK, Kim JH, Eom CY, Kim Y G, Guo M, Jung HS, Kang BS, Kim S (2015) Assembly of Multi-tRNA Synthetase Complex via Heterotetrameric Glutathione Transferase-Homology Domains. *J. Biol. Chem* **290**: 29313-29328.

- Choi JW, Kim DG, Park MC, Um JY, Han JM, Park SG, Choi EC, Kim S (2009) AIMP2 Promotes TNF-Dependent Apoptosis via Ubiquitin-Mediated Degradation of TRAF2. *J. Cell Sci* **122**: 2710-2715.
- Choi JW, Kim DG, Lee AE, Kim HR, Lee JY, Kwon NH, Shin YK, Hwang SK, Chang SH, Cho MH, Choi YL, Kim J, Oh SH, Kim B, Kim SY, Jeon HS, Park JY, Kang HP, Park BJ, Han JM, Kim S (2011) Cancer-Associated Splicing Variant of Tumor Suppressor AIMP2/p38: Pathological Implication in Tumorigenesis. *PLoS Genet* **7**: e1001351.
- Choi JW, Lee JW, Kim, JK, Jeon HK, Choi JJ, Kim DG, Kim BG, Nam DH, Kim HJ, Yun S H, Kim S (2012) Splicing Variant of AIMP2 as an Effective Target against Chemoresistant Ovarian Cancer. *J. Mol. Cell Biol* **4**: 164-173.
- Crespo YX, Aguilar GC, Jacomin AC, Journet A, Mortier M, Taillebourg E, Soleilhac E, Weissenhorn W, Fauvarque MO (2018) CHMP1B is a Target of USP8/UBPY Regulated by Ubiquitin During Endocytosis. *PLoS Genet* **14**: e1007456.
- Dixon AS, Schwinn MK, Hall MP, Zimmerman K, Otto P, Lubben TH, Butler BL, Binkowski BF, Machleidt T, Kirkland TA, Wood MG, Eggers CT, Encell LP, Wood KV (2016) NanoLuc Complementation Reporter Optimized for Accurate Measurement of Protein Interactions in Cells. *ACS Chem. Biol* **11**: 400-408.
- Essmann U, Perera L, Berkowitz ML, Darden T, Lee H, Pedersen LG (1995) A Smooth Particle Mesh Ewald Method. *J. Chem. Phys* **103**: 8577-8593.
- Han JM, Park BJ, Park SG, Oh YS, Choi SJ, Lee SW, Hwang SK, Chang SH, Cho MH, Kim S (2008) AIMP2/p38, the Scaffold for the Multi-tRNA Synthetase Complex, Responds to Genotoxic Stresses via p53. *Proc. Natl. Acad. Sci. U. S. A.* **105**: 11206-11211.
- Hess B, Bekker H, Berendsen HJC, Fraaije JGEM (1997) LINCS: A Linear Constraint Solver for Molecular Simulations. *J. Comput. Chem* **18**: 1463-1472.

- Hoover WG (1985) Canonical Dynamics: Equilibrium Phase-Space Distributions. *Phys. Rev. A* **31**: 1695-1697.
- Ivanov AA, Khuri FR, Fu H (2013) Targeting Protein–Protein Interactions as an Anticancer Strategy. *Trends Pharmacol. Sci* **34**: 393-400.
- Jo S, Kim T, Iyer VG, Im W (2008) CHARMM-GUI: A Web-Based Graphical User Interface for CHARMM. *J. Comput. Chem* **29**: 1859-1865.
- Kim DG, Lee JY, Lee JH, Cho HY, Kang BS, Jang SY, Kim MH, Guo M, Han JM, Kim SJ, Kim S (2016) Oncogenic Mutation of AIMP2/p38 Inhibits Its Tumor-Suppressive Interaction with Smurf2. *Cancer Res* **76**: 3422-3436.
- Kim MJ, Park BJ, Kang YS, Kim HJ, Park JH, Kang JW, Lee SW, Han J. M, Lee HW, Kim S (2003) Downregulation of FUSE-Binding Protein and c-myc by tRNA Synthetase Cofactor p38 is required for Lung Cell Differentiation. *Nat. Genet* **34**: 330-336.
- Kim S, You S, Hwang D (2011) Aminoacyl-tRNA Synthetases and Tumorigenesis: More Than Housekeeping. *Nat. Rev. Cancer* **11**: 708-718.
- Kumari R, Kumar R. (2014) Open Source Drug Discovery Consortium; Lynn, A. g_mmpbsa-A GROMACS tool for high-throughput MM-PBSA calculations. *J. Chem. Inf. Model* **54**: 1951-1962.
- Langhans SA (2018) Three-Dimensional in vitro Cell Culture Models in Drug Discovery and Drug Repositioning. *frontiers in Pharmacology* **9**: 1-14.
- Lee HS, Kim DG, Oh YS, Kwon NH, Lee JY, Kim D, Park SH, Song JH, Lee S, Han JM, Park BJ, Lee J, Kim S (2013) Chemical Suppression of an Oncogenic Splicing Variant of AIMP2 Induces Tumour Regression. *Biochem J* **454**: 411-416.
- Li Z, Ivanov AA, Su R, Gonzalez PV, Qi Q, Liu S, Webber P, McMillan E, Rusnak L, Pham C, Chen X, Mo X, Revennaugh B, Zhou W, Marcus A, Harati S, Chen X, Johns M.A,

- White M A, Moreno CS, Cooper LAD, Du Y, Khuri FR, Fu H (2017) The OncoPPI Network of Cancer-Focused Protein–Protein Interactions to Inform Biological Insights and Therapeutic Strategies. *Nat. Commun* **8**: 14356.
- Lim S, Cho HY, Kim DG, Roh Y, Son SY, Mushtaq AU, Kim M, Bhattarai D, Sivaraman A, Lee Y, Lee J, Yang WS, Kim HK, Kim MH, Lee K, Jeon YH, Kim S (2019) Targeting the Interaction of AIMP2-DX2 with HSP70 Suppresses Cancer Development. *Nat. Chem. Biol* **16**: 31-41.
- Lim S, Kim DG, Kim S (2019) ERK-Dependent Phosphorylation of the Linker and Substrate-Binding Domain of HSP70 Increases Folding Activity and Cell Proliferation. *Exp. Mol. Med* **51**: 1-14.
- Miyatake OH, Barrett AGM (2013) Synthetic Studies Towards Tragoponol: Preparation of a Highly Functionalized Resorcyate. *Tetrahedron Lett* **54**: 4817-4820.
- Nero TL, Morton CJ, Holien JK, Wielens J, Parker MW (2014) Oncogenic Protein Interfaces: Small Molecules, Big Challenges. *Nat. Rev. Cancer* **14**: 248-262.
- Oh AY, Jung YS, Kim J, Lee JH, Cho JH, Chun HY, Park S, Park H, Lim S, Ha N C, Park JS, Park CS, Song GY, Park BJ (2016) Inhibiting DX2-p14/ARF Interaction Exerts Antitumor Effects in Lung Cancer and Delays Tumor Progression. *Cancer Res* **76**: 4791-4804.
- Park MC, Jeong H, Son SH, Kim Y, Han D, Goughnour PC, Kang T, Kwon NH, Moon HE, Paek SH, Hwang D, Seol HJ, Nam DH, Kim S (2016) Novel Morphologic and Genetic Analysis of Cancer Cells in a 3D Microenvironment Identifies STAT3 as a Regulator of Tumor Permeability Barrier Function. *Cancer Res* **76**: 1044-1054.
- Parrinello M, Rahman A (1981) Polymorphic Transitions in Single Crystals: A New Molecular Dynamics Method. *J. Appl. Phys* **52**: 7182-7190.

- Ran X, Gestwicki JE (2018) Inhibitors of Protein–Protein Interactions (PPIs): An Analysis of Scaffold Choices and Buried Surface Area. *Curr. Opin. Chem. Biol* **44**: 75-86.
- Sun BF, Hong R, Kang YB, Deng L (2009) Asymmetric Total Synthesis of (–)-Plicatic Acid via a Highly Enantioselective and Diastereoselective Nucleophilic Epoxidation of Acyclic Trisubstituted Olefins. *J. Am. Chem. Soc* **131**: 10384-10385.
- Touti F, Gates ZP, Bandyopadhyay A, Lautrette G, Pentelute BL (2019) In-Solution Enrichment Identifies Peptide Inhibitors of Protein–Protein Interactions. *Nat. Chem. Biol* **15**: 410-418.
- Tribello GA, Bonomi M, Branduardi D, Camilloni C, Bussi G (2014) PLUMED 2: New Feathers for an Old Bird. *Comput. Phys. Commun* **185**: 604-613.
- Vanommeslaeghe K, Hatcher E, Acharya C, Kundu S, Zhong S, Shim J, Darian E, Guvench, O, Lopes P, Vorobyov I, Mackerell AD (2010) CHARMM General Force Field: A Force Field for Drug-Like Molecules Compatible with the CHARMM All-Atom Additive Biological Force Fields. *J. Comput. Chem* **31**: 671-690.
- Wójcik P, Berlicki L (2016) Peptide-Based Inhibitors of Protein–Protein Interactions. *Bioorg. Med. Chem. Lett* **26**: 707-713.
- Wu G, Robertson DH, Brooks CL, Vieth M (2003) Detailed Analysis of Grid-Based Molecular Docking: A Case Study of CDOCKE-A CHARMM-Based MD Docking Algorithm. *J. Comput. Chem* **24**: 1549-1562.
- Yum MK, Kang JS, Lee AE, Jo YW, Seo JY, Kim HA, Kim YY, Seong J, Lee EB, Kim JH, Han JM, Kim S, Kong YY (2016) AIMP2 Controls Intestinal Stem Cell Compartments and Tumorigenesis by Modulating Wnt/ β -Catenin Signaling. *Cancer Res* **76**: 4559-4568.

Footnotes.

This work was supported by Global Frontier Project grants (NRF-M3A6A4-2010-0029785 and NRF-2013M3A6A4944802), an IMRCTR grant (NRF-2018R1A5A2023127) of the National Research Foundation, and SI-1951-30 funded by the Ministry of Science and ICT (MSIT).

Conflict of interest

All authors disclose no conflict of interest.

Figure Legends

Figure 1. Identification of compound **1**, a PPI inhibitor of DX2 and HSP70. (a) NanoBiT-based screening system. (b) Flow chart of the binding inhibitor screening. Ninety-nine chemicals showing over 60% inhibition at 5 μM were selected from the primary screening. To examine the specificity, we used the binding pair PRKACA and PRKAR2A as a secondary screening, and 10 chemicals were chosen. (c) Comparison of the inhibitory effects of the 10 chemicals (10 μM) on the binding of DX2-HSP70 and PRKACA-PRKAR2A via the NanoBiT assay. (d) Inhibitory efficacy of the chemicals on the direct binding of DX2 and HSP70 determined by an *in vitro* pull-down assay. Quantified values of binding are presented at the bottom of the gel image. (e) Cell viability was determined upon treatment with the 10 chemicals (10 μM) in DX2-inducible A549 cells. DX2 was induced by treatment with doxycycline (dox). (f) Structure of compound **1**. * The experiments in (c) and (e) were independently repeated three times with error bars denoting the standard deviation (S.D.). Student's two-tailed t-test was performed for statistical analysis (* $P < 0.05$, ** $P < 0.01$ and *** $P < 0.005$).

Figure 2. Preparation of the Biotinylated Compound **15**

Reagents and conditions: (a) BBr_3 2 equiv, CH_2Cl_2 , -15°C , 1.5 h, 82%; (b) piperidine 0.5 equiv, benzaldehyde 1.2 equiv, toluene, reflux, 43 and 25%; (c) $(\text{COCl})_2$ 1 equiv, cat. dimethylformamide (DMF), CH_2Cl_2 , 0°C ; (d) pyridine 1 equiv, CH_2Cl_2 , rt, overnight, 10%

Figure 3. Characterization of compound **1**. (a) NanoBiT assay for the binding between DX2 and HSP70 and the binding between PRKACA and PRKAR2A upon treatment with compound **1**. The experiments were independently repeated three times with error bars denoting the S.D. Student's two-tailed t-test was performed for statistical analysis (*** $P < 0.005$). (b) Inhibitory effects of compound **1** on the endogenous binding of DX2 with HSP70. HSP70 (left) or DX2 (right) from the same cells were precipitated with a specific antibody. Actin was used as a loading control. (c) *In vitro* pull-down assay showing the inhibitory effects of compound **1** on the interaction between DX2 and HSP70. Quantified values of binding are presented at the bottom of the gel image. (d) H460 cells were treated with compound **1**, and then the chemicals were removed by addition of fresh medium at the indicated time. The cells were precipitated by using an anti-HSP70 antibody. (e) Protein and mRNA levels from H460 cells treated with compound **1**. (f) Ubiquitination assay of H460 cells treated with compound **1**. (g) Significance of Siah1 on HSP70- or compound **1**-dependent DX2 levels. H460 cells knocked down by introducing specific si-Siah1 were ectopically expressed with HSP70 (upper) or treated with compound **1** (bottom). * (b), (c), (d), (e), (f) and (g) The quantification of the protein level for each experiment is presented at the bottom of each blot.

Figure 4. Direct binding of compound **1** to DX2. (a) Direct binding of **1** to DX2. The purified DX2 or HSP70 proteins were mixed with **15** or biotin. Biotin was used as a negative control. (b) Specific binding of **1** to DX2, not HSP70. The proteins DX2 and HSP70 were incubated with **15**, and **1** was additionally added. (c) Specific binding of **1** to endogenous DX2. H460

cells were treated with biotin, **15** or **1** as indicated and analyzed by immunoblotting. (d) SPR analysis for calculating the binding affinity between DX2 and **1**. (e) Determination of the domain responsible for the binding between **1** and DX2. The DX2 protein was divided as shown on the right.

Figure 5. Prediction and validation of the binding site of compound **1**. (a) Distance distribution of **1** with three significant residues displaying stable interactions during the last 200 ns. The blue, magenta and green lines represent the distances of ligand:O3, ligand:C13 and ligand:O1 towards K129:NZ, Y47:CG and N56:ND2, respectively. Compound **1** is represented as green sticks. (b) Binding mode of **1** with DX2 obtained from the molecular modeling study. The electrostatic surface model of DX2 taken from the representative structure at 211.3 ns (right) and the zoomed-in view showing the detailed interactions with **1** (green) with the three significant binding residues (red) shown by the stick model (left). (c) Binding of **1** to DX2 *via* mutagenesis studies. Cell extracts expressing each of the FLAG-tagged DX2 mutants were mixed with **15** and subjected to an *in vitro* pull-down assay. PD denotes pull-down. (d) DX2-HSP70 binding inhibition of **1** *via* mutagenesis studies. 293T cells expressing FLAG-tagged DX2 were incubated with or without **1** for 6 h and then subjected to immunoprecipitation. Actin was used as a loading control. The quantification of the protein level for each experiment is presented as a bar graph on the right of (c) and (d). (e) Ubiquitination assay using DX2 mutants. The amounts of ubiquitinated DX2 were assessed by SDS-PAGE and immunoblotting using an anti-Ub antibody. * The quantification of the protein level for each experiment is presented as a bar graph on the right of (c) and (d).

Figure 6. Determination of the mode of action of compound **1**. (a) Distance distribution of L50 in the NFR and T117 in the GST-N of DX2. The red and blue lines indicate the results obtained from the apo and chemical-bound systems, respectively. (b) The representative

structure of chemically bound DX2 showing that the binding region with HSP70 can be masked by significant hydrophobic interactions. The key residues of DX2 (gray) and **1** (green) are represented as the van der Waals (vdW) model. (c) The proposed binding models of DX2 and HSP70 (upper) and DX2 and **1** (bottom). The DX2-NFR (residues 1-50) is depicted as a line in the absence of **1** (upper), but the NFR (residues 38-50) is represented as a surface to highlight the bumping region in the presence of **1** (bottom). The structures of DX2 and HSP70 are shown as electrostatic and yellow surfaces, respectively.

Figure 7. Inhibitory effects of compound **1** on cancer cell proliferation. (a) Cell viability assay on various normal and cancerous lung cells. Each color indicates the different protein levels of DX2 (red: high, blue and green: median, yellow: low) (Supplementary Figure S5a). (b) Inhibition of H460 cell spheroids in 3D culture conditions upon treatment with **1** (96 h). Cell viability was determined by a CellTiter-Glo 3D assay. (c) The effect of **1** on the *in vivo* cancer development model. A total of 5 or 10 mg/kg **1** was intraperitoneally administered for 10 days every other day to mice ($n=3$) subcutaneously embedded with H460 cells. Tumor size was monitored for the injection period (left). The weights of the excised tumors are shown as a bar graph (middle). Representative images of mice bearing tumors and the excised tumors are shown (right). (d) Cell viability assays using A549 cells stably expressing the indicated DX2 mutants treated with **1**. Red and blue colors indicate WT and mutants of DX2, respectively. (e) Anchorage-independent colony-forming assay using H460 cells stably expressing DX2 WT or mutants treated with **1**. Representative images are shown on the right. * The experiments were independently repeated three times with error bars denoting the S.D. in (a), (b), (d) and (e). Student's two-tailed t-test was performed for statistical analysis (* $P < 0.05$, ** $P < 0.01$ and *** $P < 0.005$).

Table 1. Inhibitory Effects of Derivatives of Compound **1** on the DX2-HSP70 and PRKACA-PRKAR2A Interactions.

Cmpd	R ¹	R ²	R ³	% Inhibition (5 μM)	
				DX2-HSP70	PRKACA-PRKAR2A
1		OEt		59.95±2.66	17.95±2.55
2		OEt		66.12±4.18	20.89±2.38
3		OEt		76.31±2.36	7.45±6.66
4		OEt		53.27±6.72	13.96±2.55
5				55.69±5.40	19.57±5.22
6				34.45±6.31	11.70±7.12
7				49.43±4.33	23.00±3.54
8	CF ₃			57.53±3.11	27.90±2.32
9	CH ₃	CH ₃		57.53±3.11	27.90±2.32

Table 2. Inhibitory Effects of Quaternary Derivatives of Compound **1** on the DX2-HSP70 Interactions.

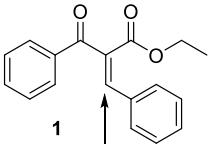
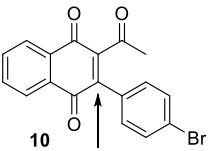
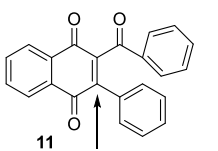
Compound	 1 Michael Acceptor	 10 Quaternary carbon	 11 Quaternary carbon
% Inhibition (5 μ M) on DX2-HSP70	59.95	63.43	60.87

Figure 1

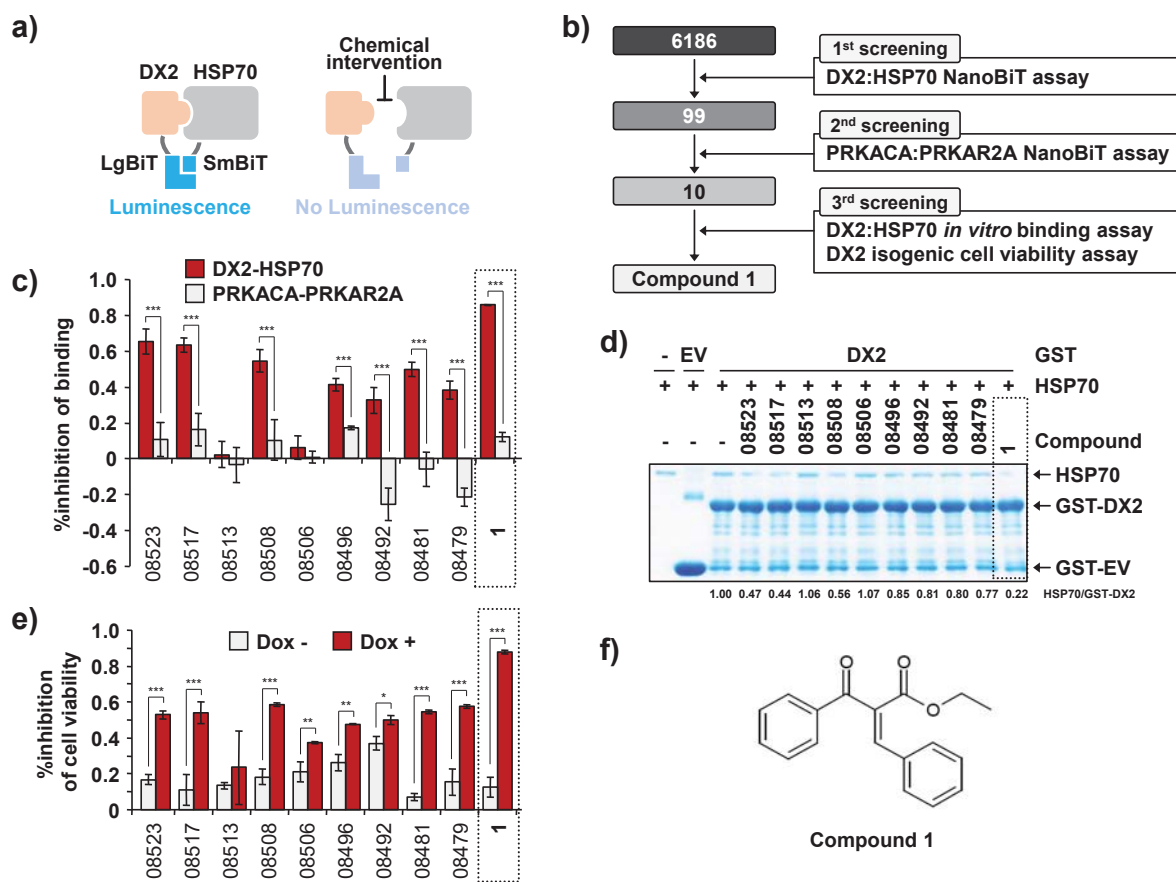


Figure 2

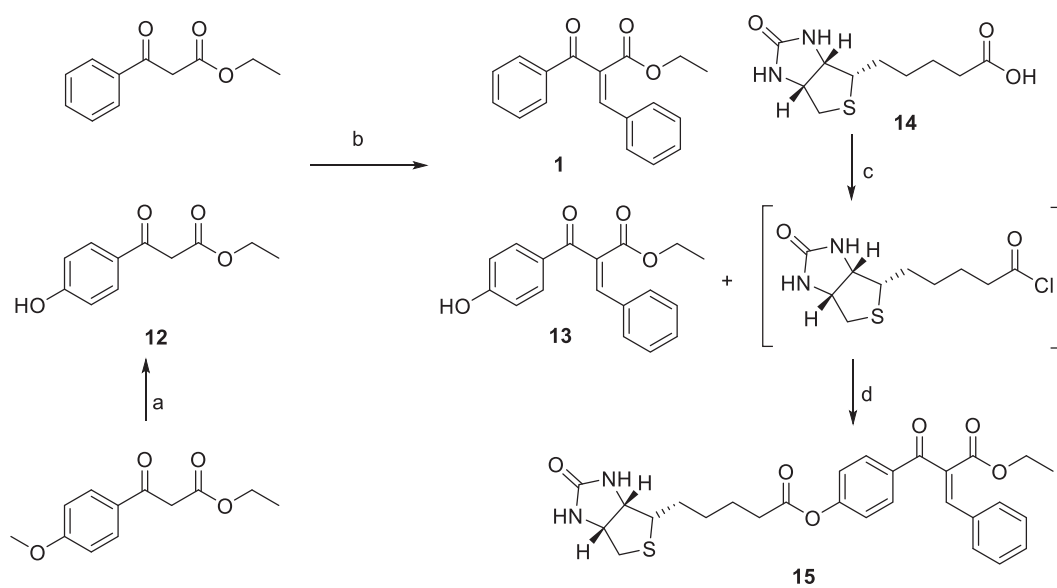


Figure 3

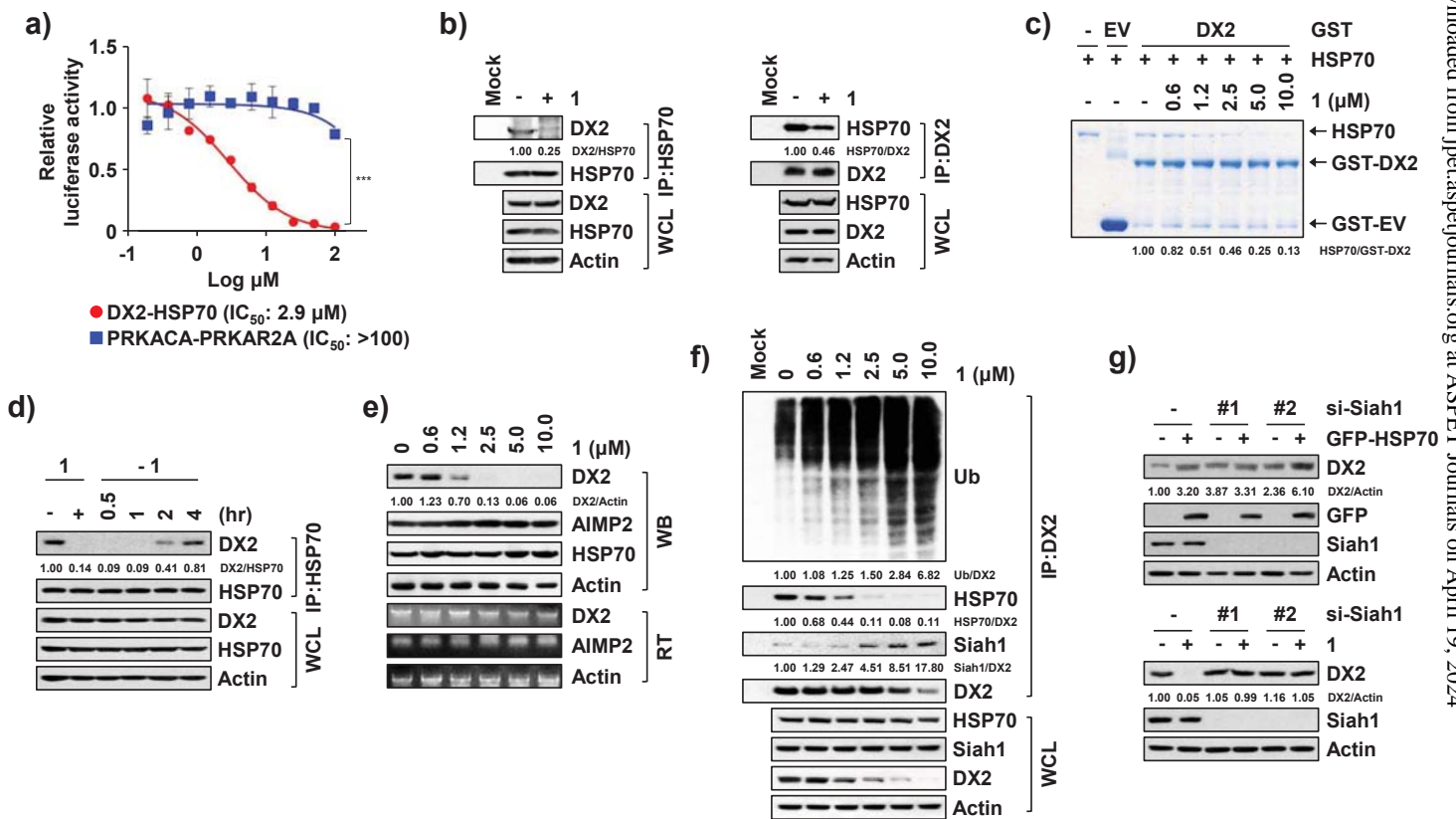


Figure 4

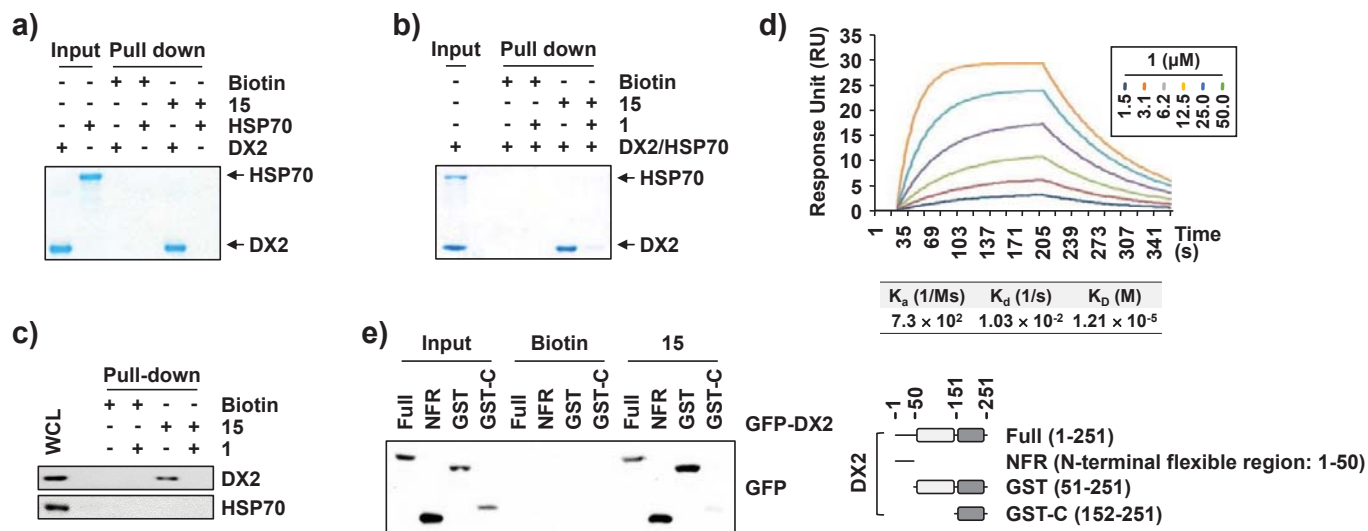


Figure 5

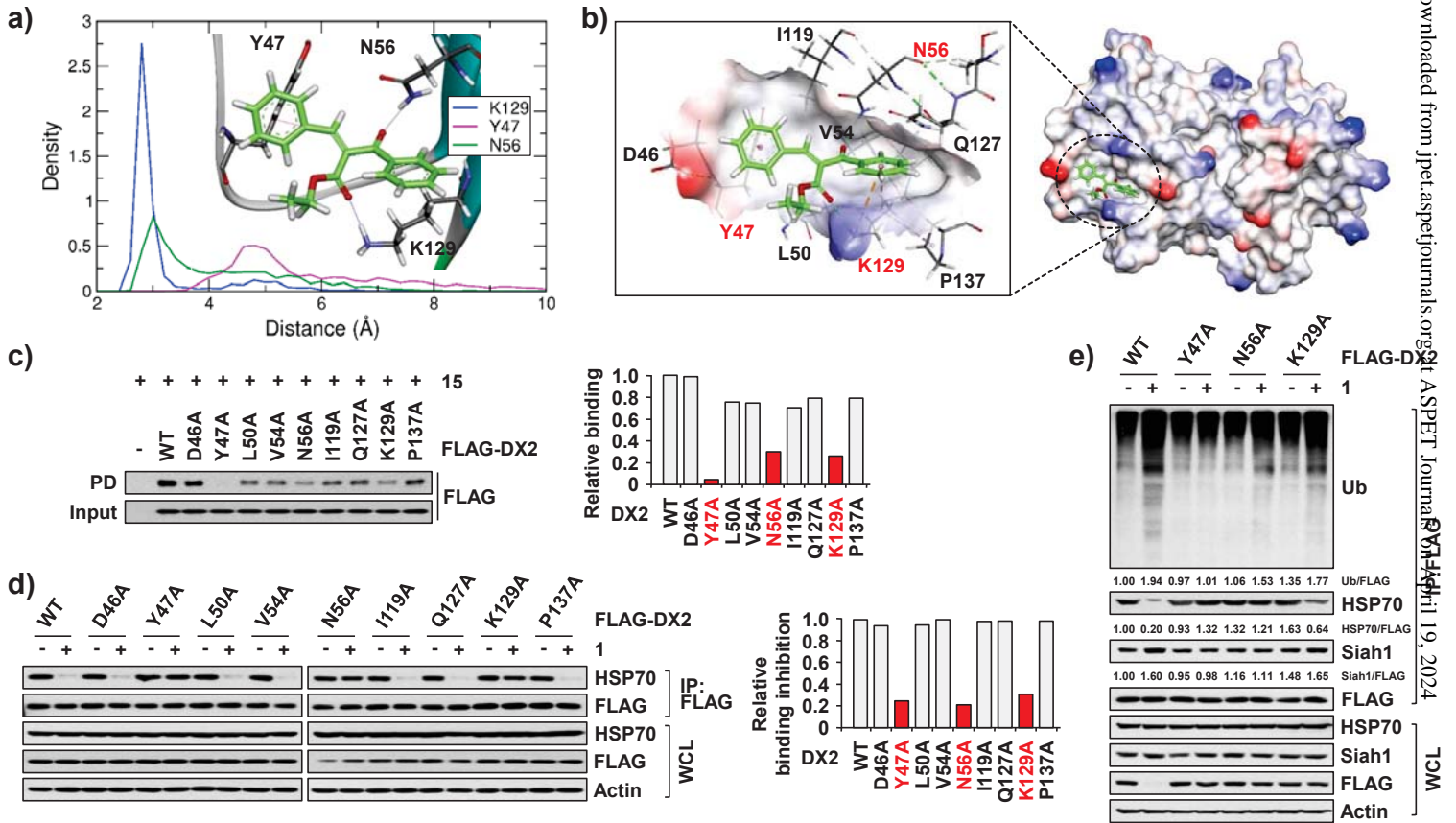


Figure 6

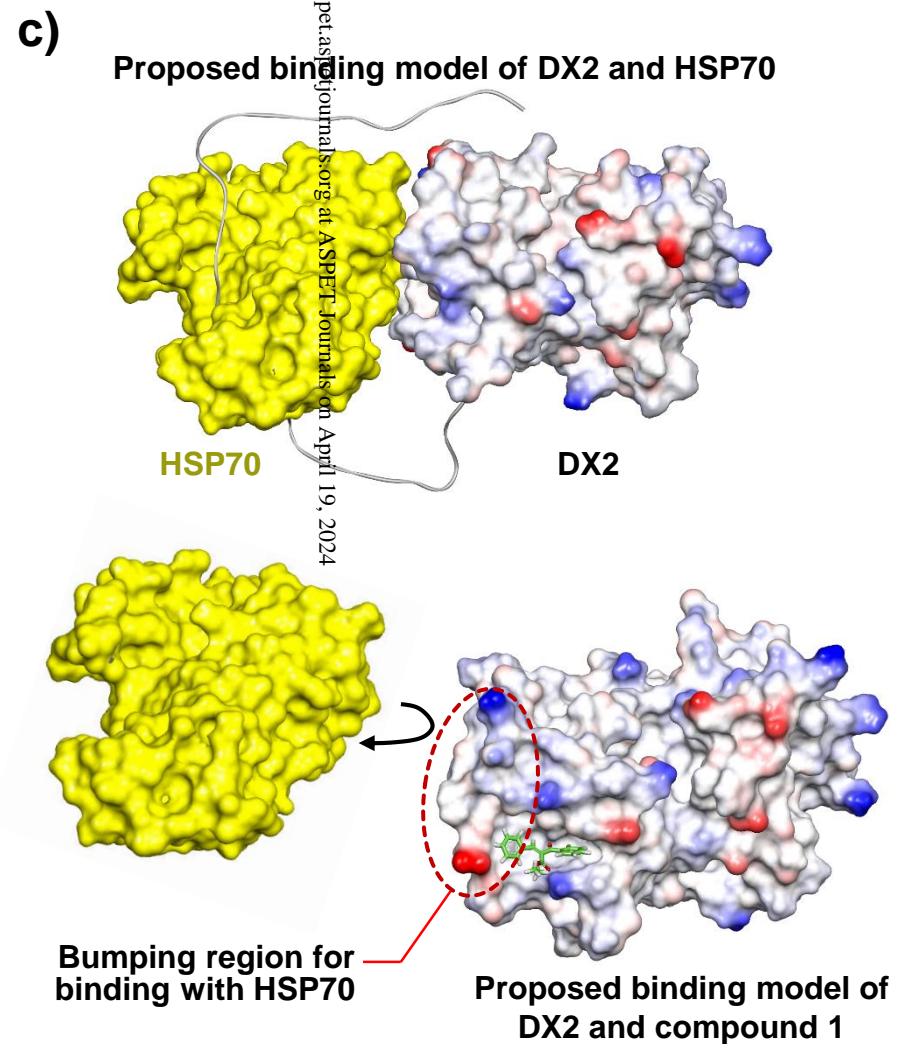
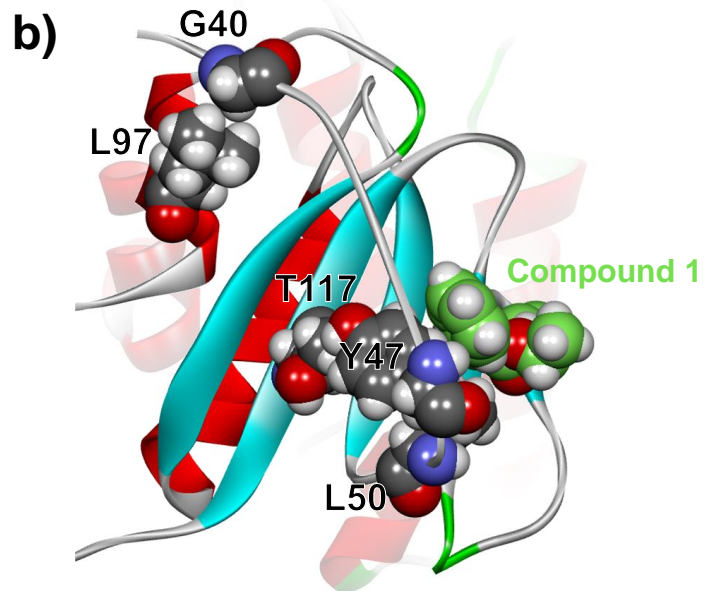
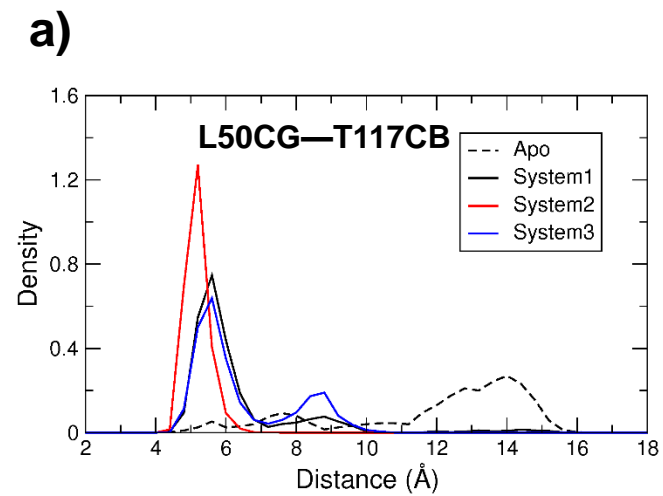
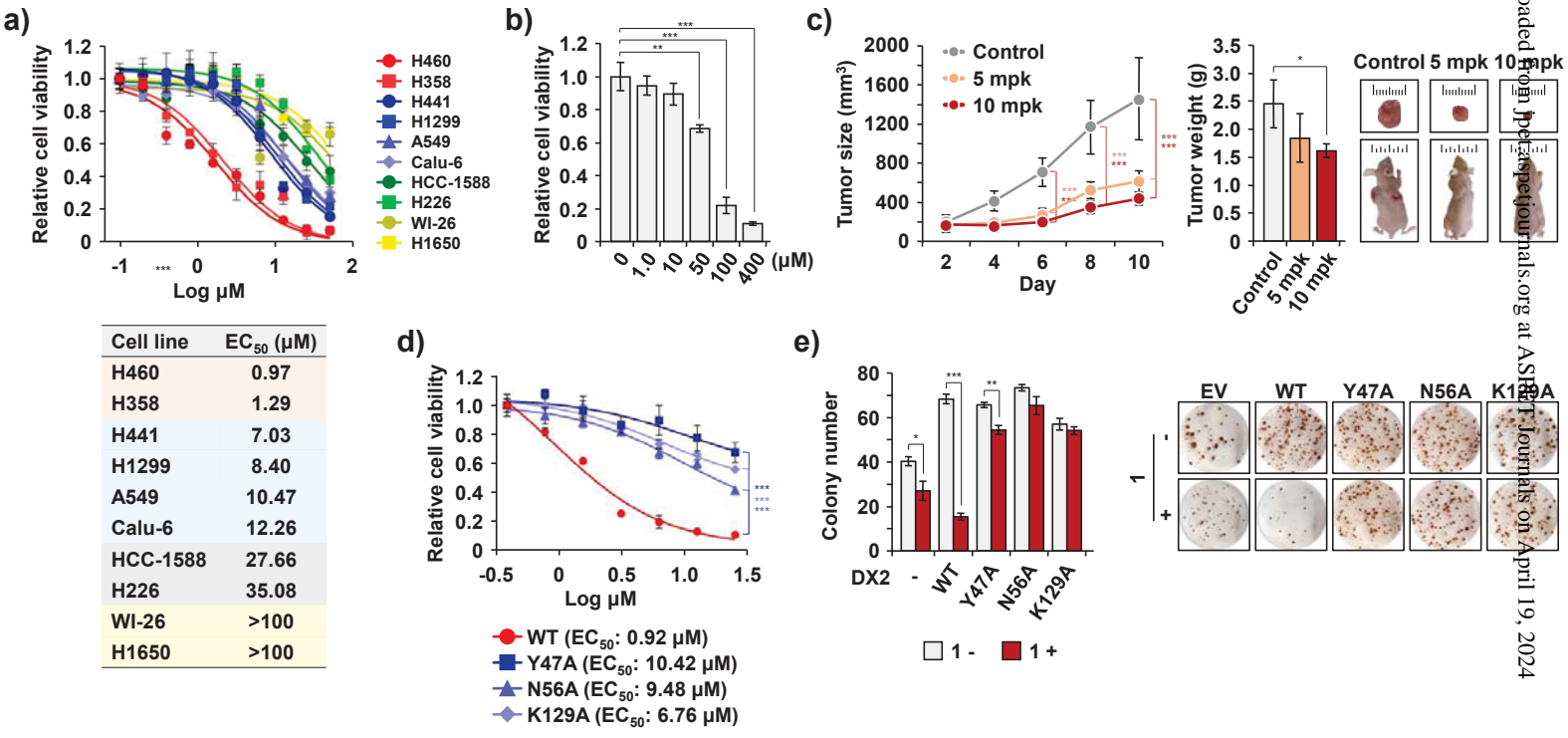


Figure 7



Allosteric Inhibition of the Tumor-Promoting Interaction between AIMP2-DX2 and HSP70

Dae Gyu Kim^{1,#}, Srigouri Huddar^{2,3,#}, Semi Lim¹, Jiwon Kong¹, Yuno Lee², Chul Min Park^{3,4}, Seungbeom Lee⁵, Young-Ger Suh^{5,6}, Minkyung Kim⁷, Kyeong Lee⁷, Sunkyung Lee^{2,3,*}, and Sunghoon Kim^{1,*}

Supplemental Data

Supplemental information include:

- 1. Supplemental table S1 and S2**
- 2. Supplemental figure S1, S2, S3, S4, and S5**
- 3. Supplemental movie legends'**
- 4. Analysis data on compounds 1 and 15**

MS data of compound **1**. (EI⁺) , MS data of compound **15**. (EI⁺)

¹H nmr of compound **1**, ¹H nmr of compound **15**,

¹³C nmr of compound **1**, ¹³C nmr of compound **15**

Supplemental table legends

Supplemental Table S1... Cytotoxicity assay on compound **1**

Supplemental Table S2. Liver microsomal phase 1 stability on compound **1** (% remaining after 30 min)..

Supplemental figure legends

Supplemental Figure S1. Primary screening heat map.

Supplemental Figure S2. Specific inhibition of binding between DX2 and HSP70 *via* compound **1**.

Supplemental Figure S3. Validation of biotin-conjugated compound **15** and specific binding of compound **1** to DX2.

Supplemental Figure S4. Molecular dynamics simulation results for the adjustment of the GST-N upon binding with compound **1**.

Supplemental Figure S5. Inhibition of cancer cell proliferation *via* compound **1**.

Supplemental movie legends

Supplemental Movie S1 and S2. MD Trajectories for binding of compound **1** within the GST-N of DX2 for the last 150 ns

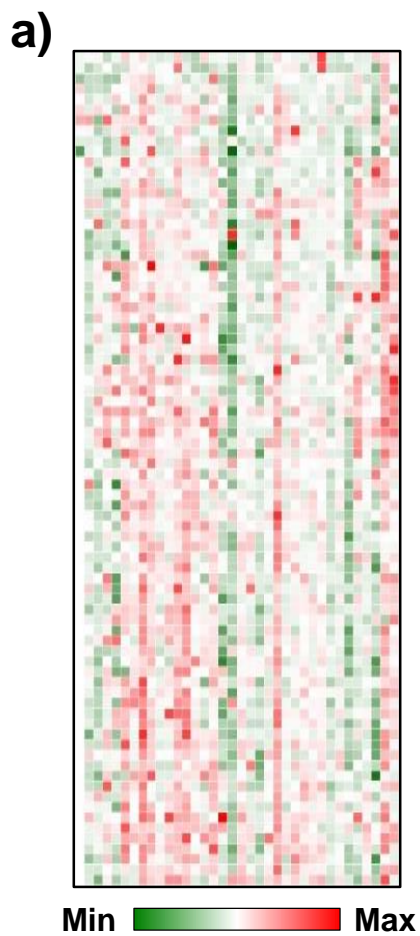
Table S1. Cytotoxicity assay on compound 1

Compounds	IC ₅₀ (μM)				
	VERO	HFL-1	L929	NIH-3T3	CHO-K1
Doxorubicin (positive control)	7.75	1.95	0.25	6.13	5.69
1	> 100	> 100	> 100	> 100	> 100

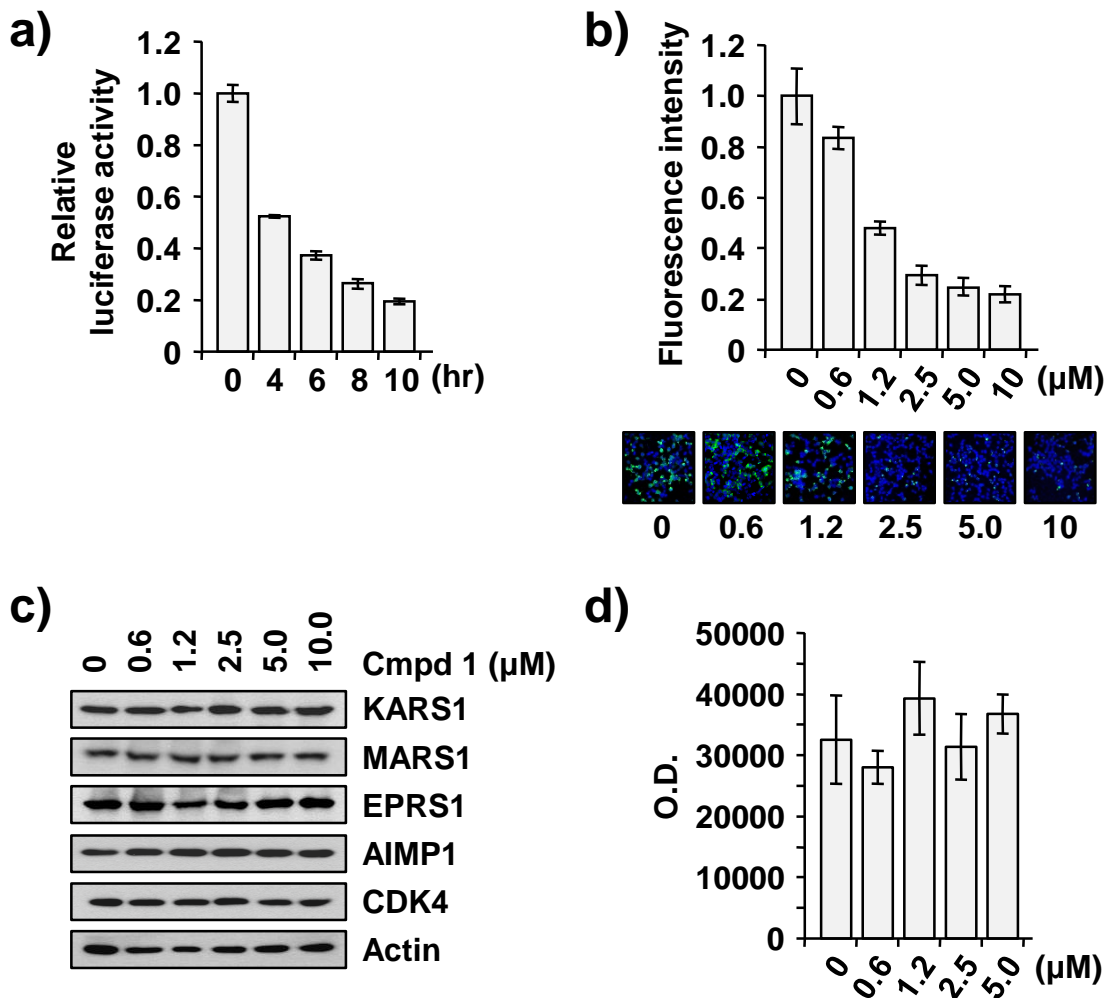
Supplemental Table S2

Table S2. Liver microsomal phase I stability (% remaining after 30 min.)

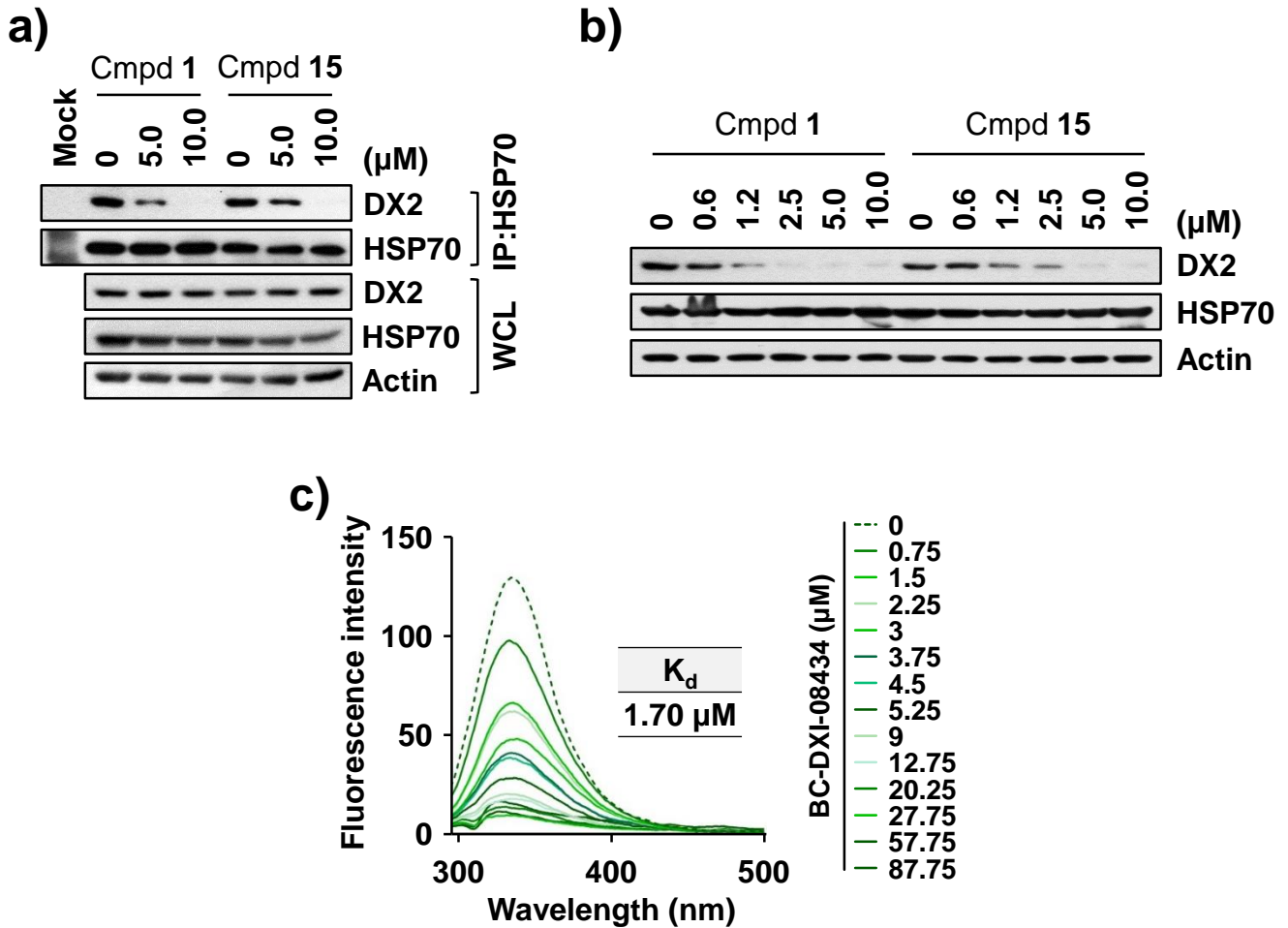
Compounds	Rat (%)	Human (%)
1	8.76%	7.02%
Buspiron (positive control)	1.1%	13.91%



Supplemental Figure S1. Primary screening heat map. (a) Heat map of primary screening results. Maximum and minimum inhibition rates were colored red and green, respectively.

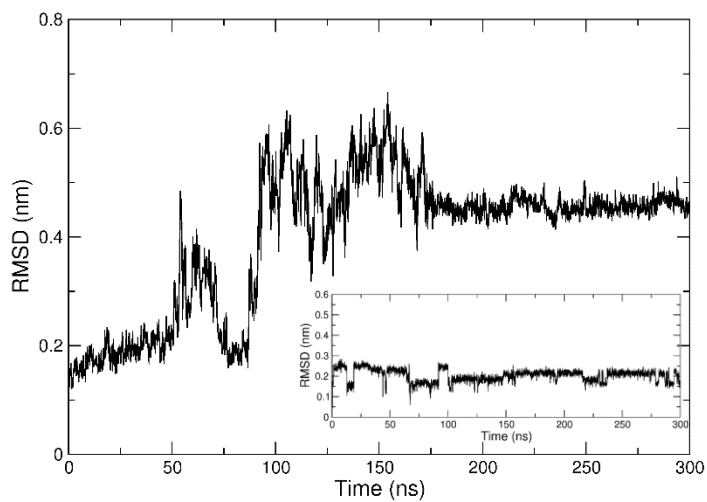


Supplemental Figure S2. Specific inhibition of binding between DX2 and HSP70 via compound 1. (a) Time-dependent inhibitory effect of BC-DXI-08434 on the binding of DX2 and HSP70. The cells expressing LgBiT-tagged DX2 and SmBiT-tagged HSP70 were treated with compound 1 (5 μM) for various treatment durations, and the luciferase signal was determined. (b) BiFC assay for checking the suppressive effect of compound 1 on the binding of DX2 and HSP70. Venus N-terminal fragment (VN)-tagged DX2 and Venus C-terminal fragment (VC)-tagged HSP70 were introduced into 293T cells, which were then treated with various doses of compound 1 for 4 h. Fluorescence estimated by confocal microscopy was quantified and shown as a graph (upper). DAPI was used to stain the nucleus. The representative images are presented below. (c) H460 cells were treated with compound 1 as indicated and subjected to SDS-PAGE and Western blotting using specific antibodies against KARS1, MARS1, EPRS1, AIMP1, CDK4 and actin. Actin was used as a loading control. (d) Effect of compound 1 on refolding activity of HSP70. A refolding assay using Glow-Fold Substrate and purified HSP70 as the substrate and chaperone, respectively, was performed with compound 1. The activity was observed by detecting the luciferase signal. (a), (b), (d) The experiments were independently repeated three times with error bars denoting S.D.

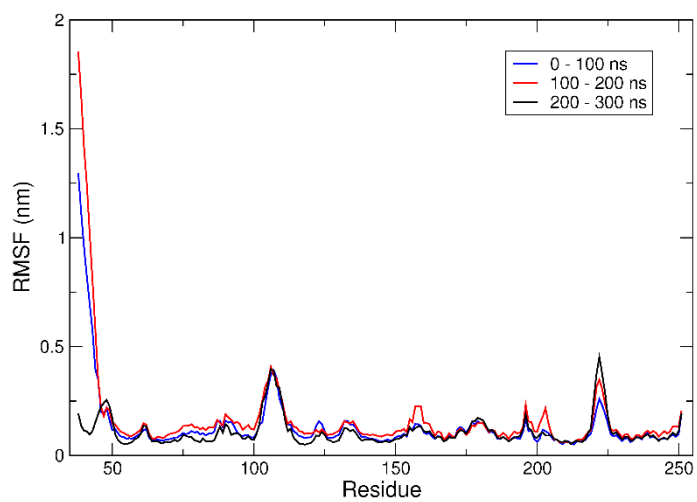


Supplemental Figure S3. Validation of biotin-conjugated compound 15 and specific binding of compound 1 to DX2. (a) H460 cells were treated with compound 1 or biotin-conjugated compound 15 in a dose-dependent manner for 4 h. HSP70 from the cell lysates was precipitated using an anti-HSP70 antibody. Coprecipitates with HSP70 were determined by SDS-PAGE and Western blotting using a specific antibody against DX2. Actin was used as a loading control. (b) H460 cells were treated with various doses of the same compounds above. The cells were subjected to SDS-PAGE and immunoblotting. (c) Binding affinity between compound 1 and DX2 proteins was determined by fluorescence-based binding titration measurements. The calculated KD value is shown.

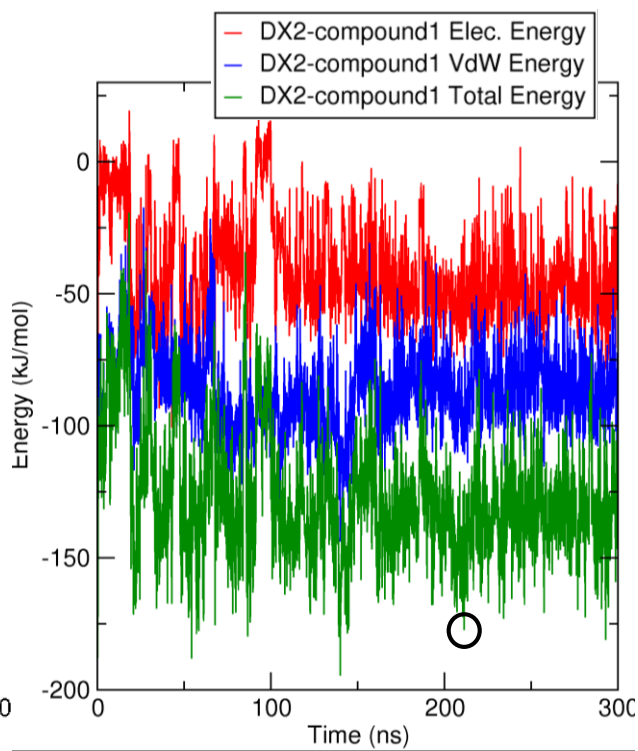
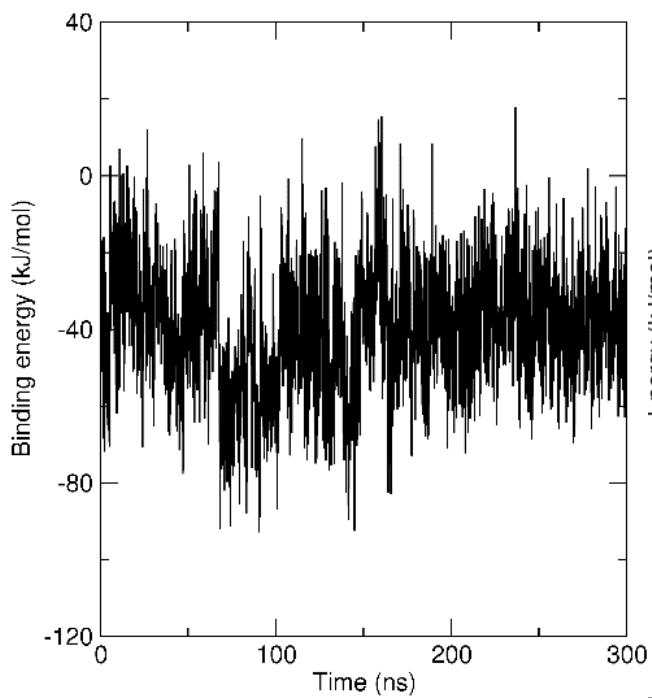
a)



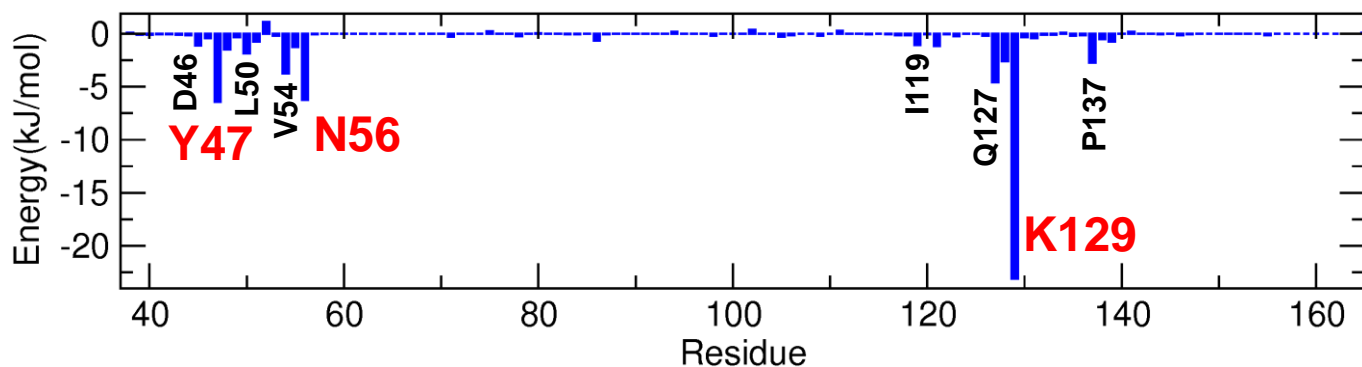
b)



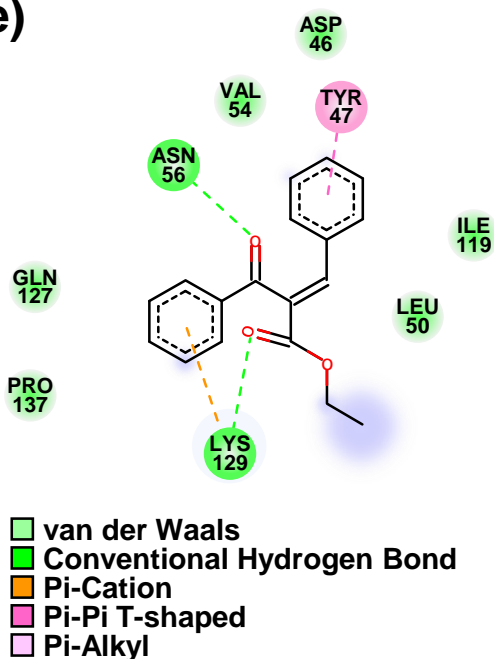
c)



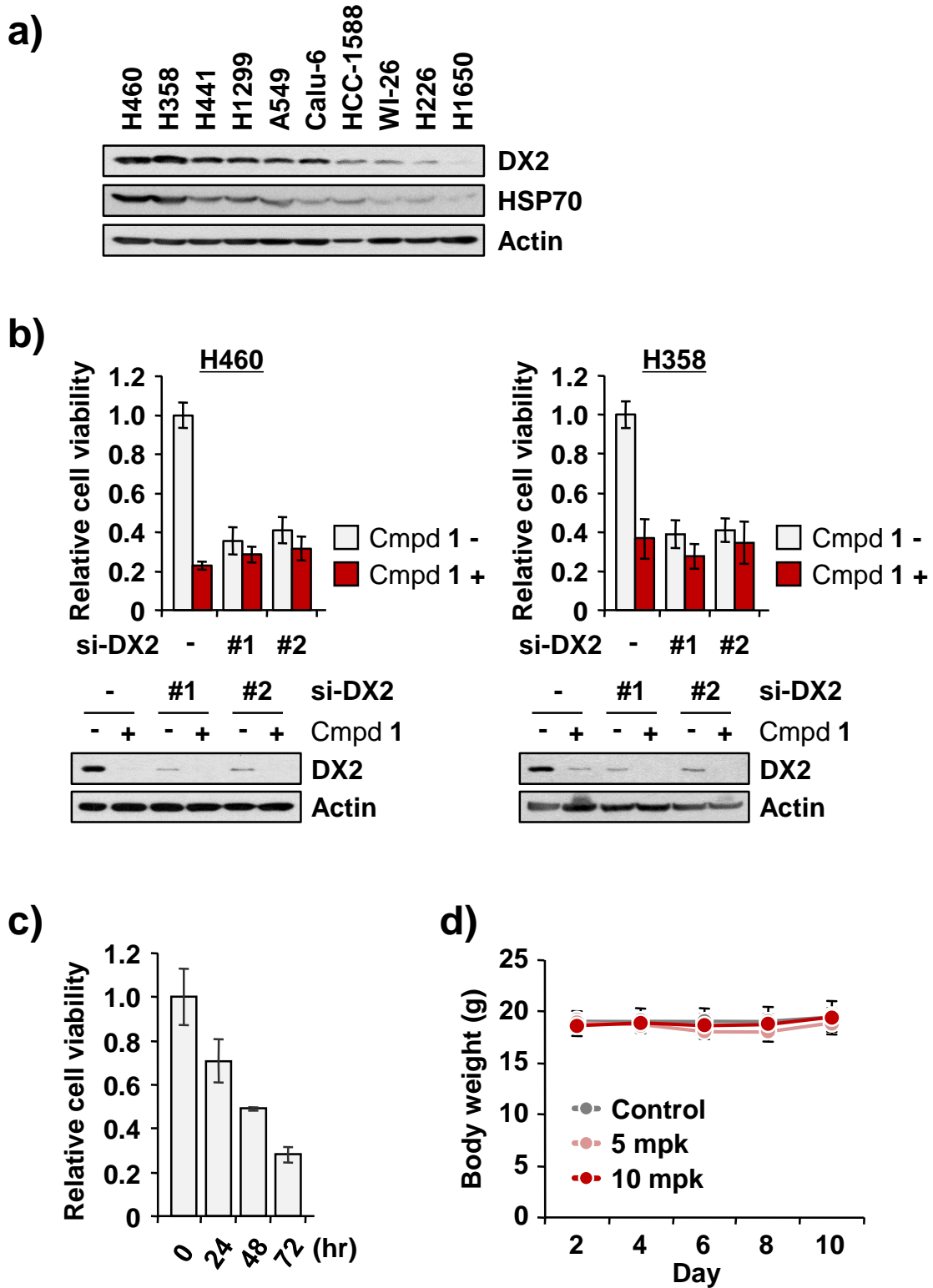
d)

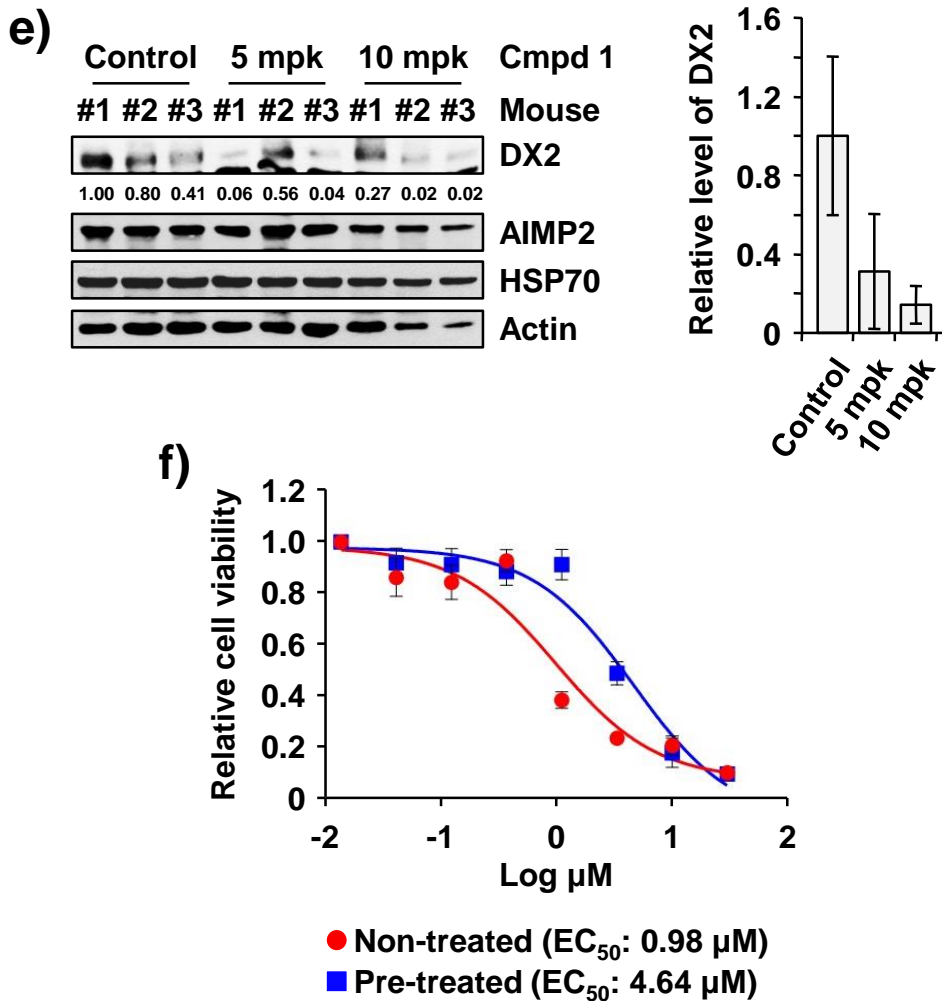


e)



Supplemental Figure S4. Molecular dynamics simulation results for the adjustment of the GST-N upon binding with compound 1. (a) $C\alpha$ -RMSD of DX2 protein and ligand RMSD of **1** (inset). (b) $C\alpha$ -RMSF of the DX2 protein with different time periods. (c) Binding energy (left) and nonbonded interaction energies (right) of **1** with DX2 calculated as a function of time. Nonbonded energies showing the maintenance of the ligand during the last 200 ns. The electrostatic, vdW and nonbond energy are displayed by red, green and blue lines, respectively. The representative frame (211.3 ns) is highlighted by black circle. (d) Non-bonded interaction energy contribution of key binding residues obtained from the per-residue energy decomposition study. (e) The interaction diagram of **1** with the interacting residues of DX2 is displayed by circles. The hydrogen bond (green) and Pi (orange and magenta) interactions are represented as dotted lines.





Supplemental Figure S5. Inhibition of cancer cell proliferation via compound 1. (a) DX2 and HSP70 protein levels in various lung normal and cancer cell lines. The levels of these two proteins were determined by immunoblotting using their specific antibodies. Actin was used as a loading control. (b) H460 and H358 cells introducing with specific si-RNA against DX2 were treated with 1. The cells were subjected to MTT (upper) and immunoblotting assay (bottom) for determining the cell viability and the level of DX2, respectively. (c) H460 cells were treated with 1 (5 μM) for various durations. The cell viability at each time point was observed by MTT assay. (d), (e) *In vivo* efficacy of 1. Compound 1 (5 and 10 mg/kg) was intraperitoneally injected into BALB/cSLC-*nu/nu* mice ($n=3$) xenografted with H460 cells (see Figure 6c). Body weight was measured over the experimental period (d). The protein levels of DX2 and HSP70 from the excised tumors were observed by immunoblotting using anti-DX2 and anti-HSP70 antibodies. DX2 level was quantified (left) and the mean value was presented as a graph (right) (e). (f) H460 cells pre-treated with 1 (0.5 μM) for three weeks were treated with 1 in dose-dependent manner and compared with the result from native H460 cells. Calculated EC_{50} were shown as below. *(b), (c), (f) The experiments were independently repeated three times with error bars denoting S.D.

Supplemental Movie S1 and S2. MD Trajectories for binding of compound 1 within the GST-N of DX2 for the last 150 ns. The structure of DX2 is shown as a ribbon (Supplemental movie S1) and surface (Supplementa movie S2) representation.

Data: 1-12-001 Date: 12-Jan-2021 09:14

Instrument: MStation

Sample: sm-840

Note: -

Inlet: Direct Ion Mode: EI+

RT: 0.54 min Scan#: 17

Elements: C 18/0, H 16/0, O 3/0

Mass Tolerance: 1000ppm, 5mmu if m/z < 5, 10mmu if m/z > 10

Unsaturation (U.S.): -0.5 - 20.0

	Observed m/z	Int%	Err [ppm / mmu]	U.S.	Composition
1	280.1102	100.00	+0.9 / +0.3	11.0	C18 H16 O3

Data : 1-14-002 Date : 14-Jan-2021 14:10

Instrument : MStation

Sample : sm-912

Note : -

Inlet : Direct Ion Mode : FAB+

RT : 1.52 min Scan# : 14

Elements : C 28/0, H 31/0, N 2/0, O 6/0, S 1/0

Mass Tolerance : 1000ppm, 5mmu if m/z < 5, 10mmu if m/z > 10

Unsaturation (U.S.) : -0.5 - 20.0

	Observed m/z	Int%	Err [ppm / mmu]	U.S.	Composition
1	523.1884	3.04	-3.6 / -1.9	15.5	C28 H31 N2 O6 S

SM-840-13-20-CDCI3.1.fid
SM-840-13-20-CDCI3

Sample : compound 1

1H NMR Spectrum of compound 1

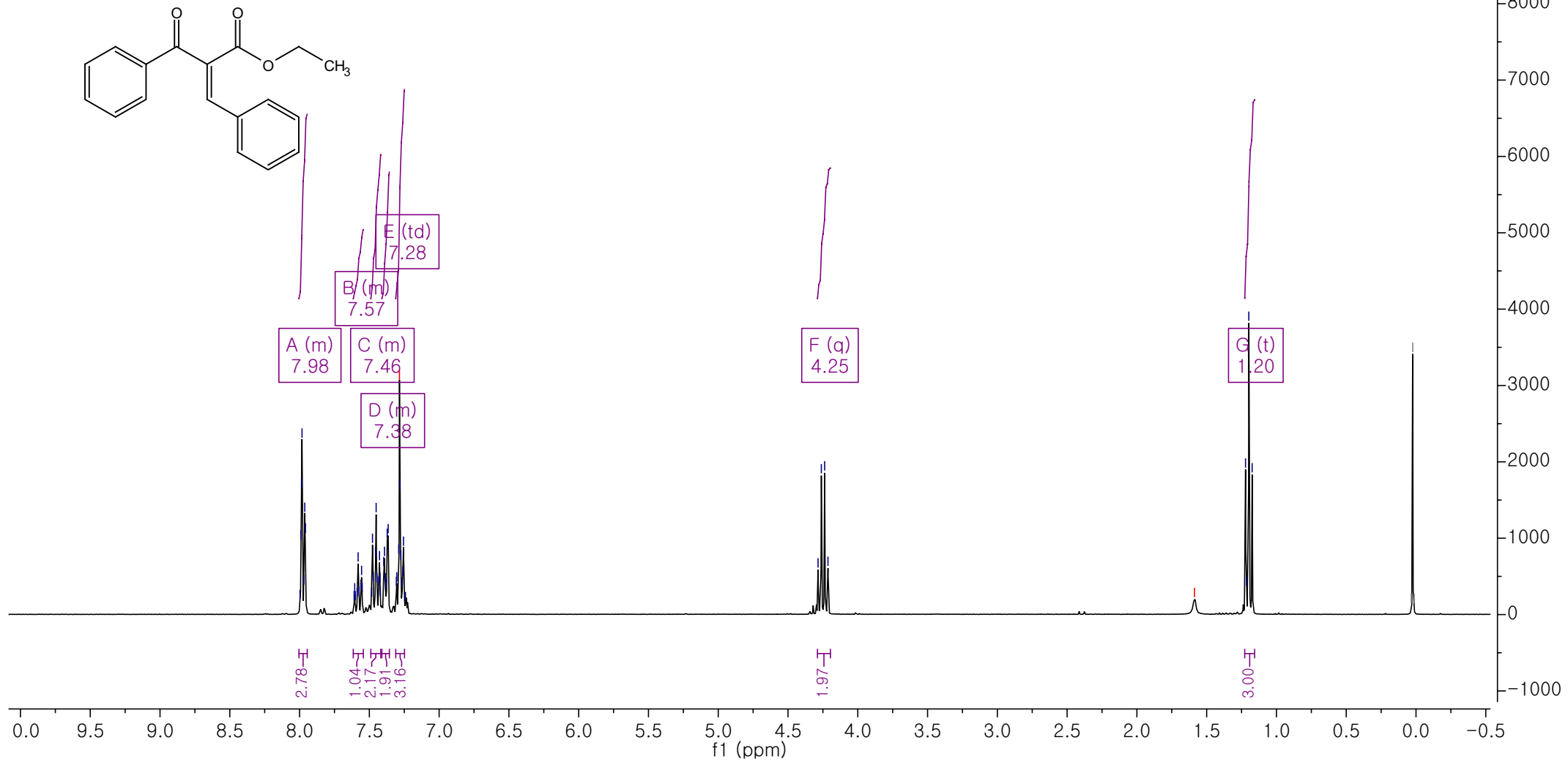
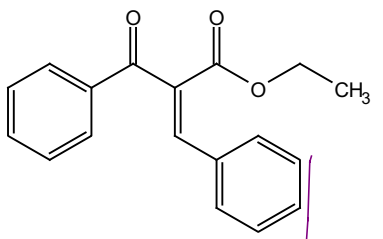
7.997
7.990
7.986
7.982
7.970
7.963
7.958
7.609
7.605
7.600
7.588
7.580
7.573
7.560
7.556
7.551
7.484
7.477
7.472
7.456
7.451
7.446
7.433
7.427
7.424
7.421
7.397
7.391
7.386
7.379
7.372
7.365
7.306
7.303
7.290
7.284 CDCl3
7.280
7.275
7.267
7.260
7.255
7.241
4.285
4.261
4.237
4.214

1.587 H2O

1.222
1.214
1.198
1.174

0.035
0.024
0.013

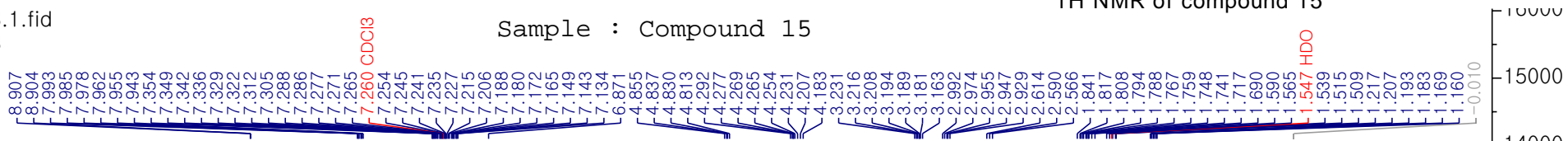
¹H NMR (300 MHz, Chloroform-*d*) δ 8.00 – 7.95 (m, 3H), 7.62 – 7.54 (m, 1H), 7.49 – 7.42 (m, 2H), 7.41 – 7.36 (m, 2H), 7.31-7.26 (m, 3H), 4.25 (q, *J* = 7.1 Hz, 2H), 1.20 (t, *J* = 7.1 Hz, 3H).



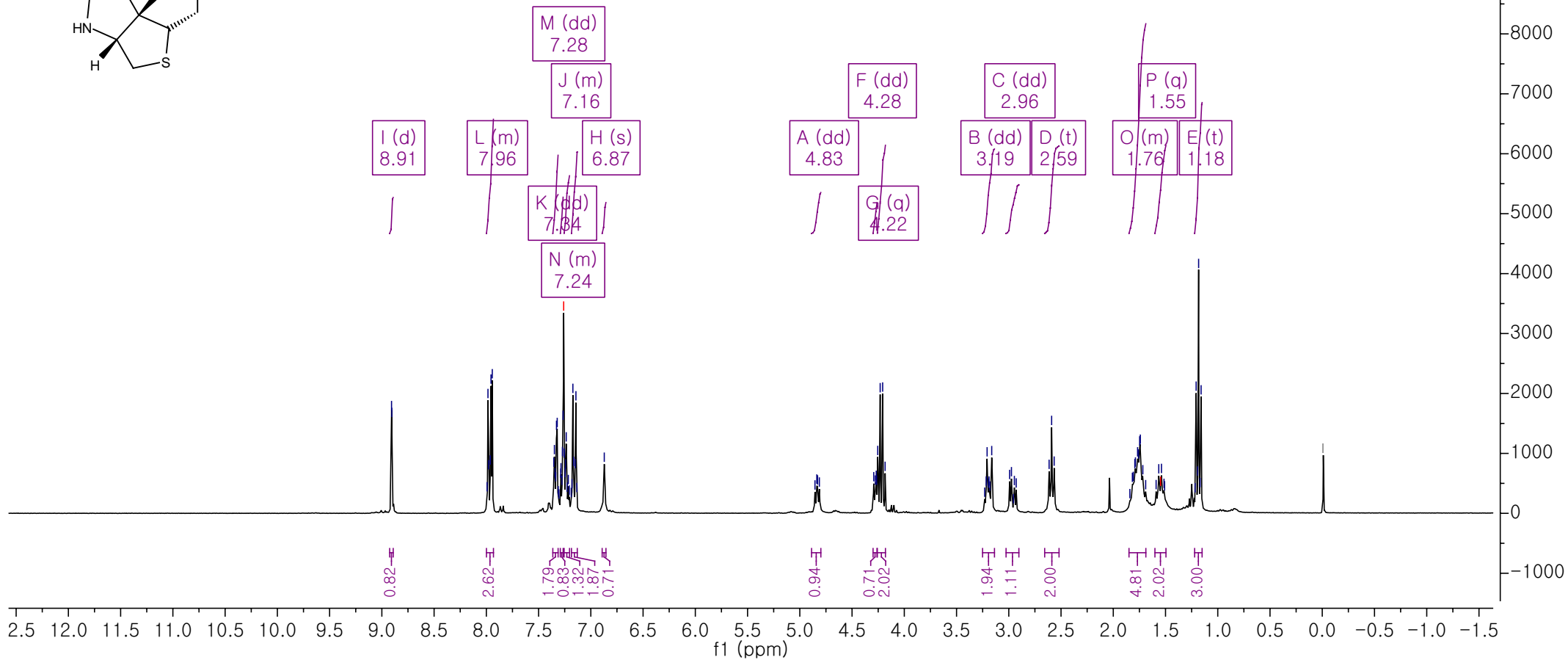
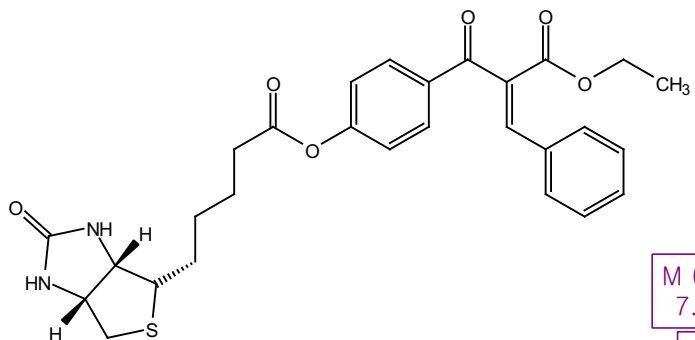
SM-858-2-CDCI3.1.fid
SM-858-2-CDCI3

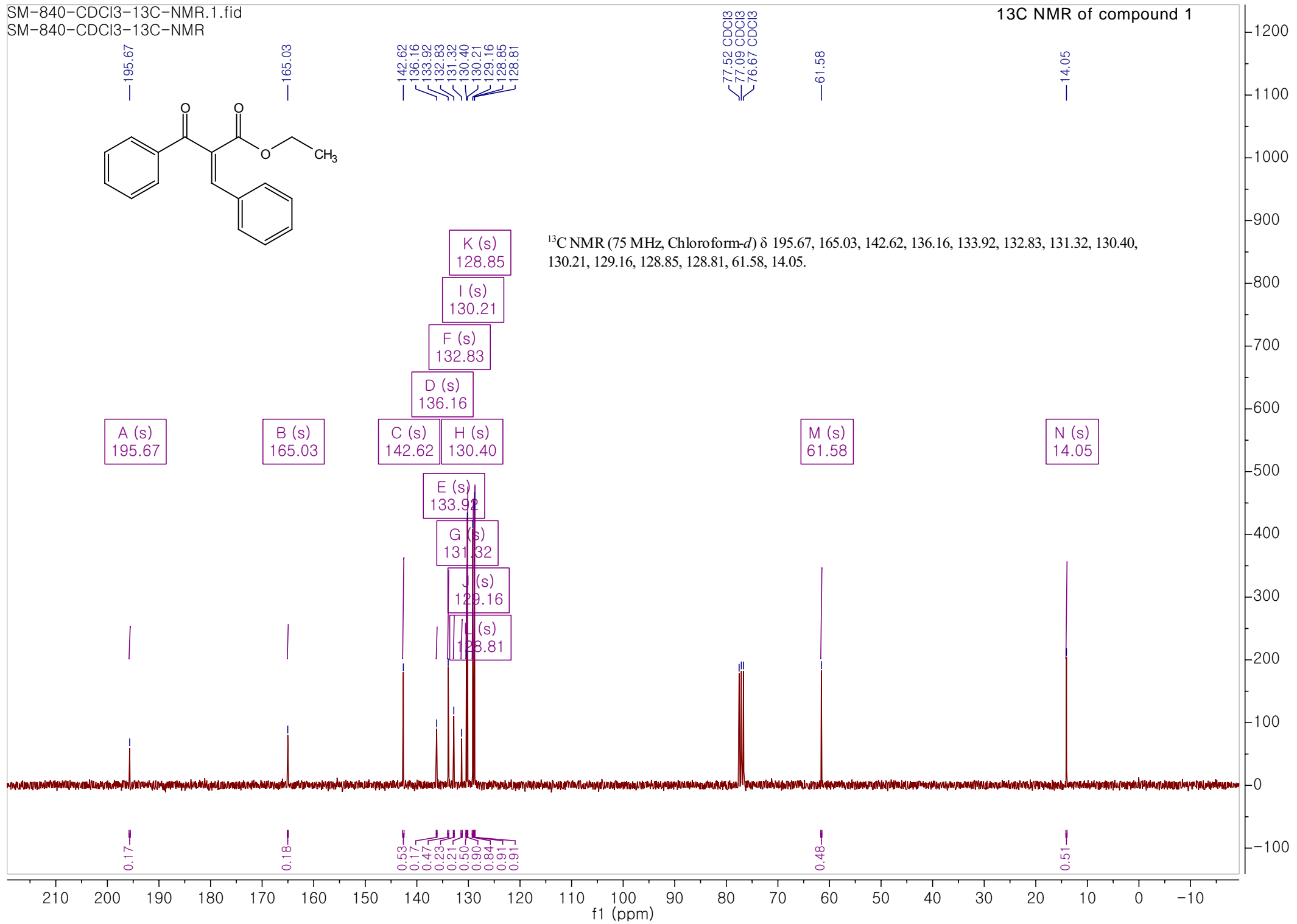
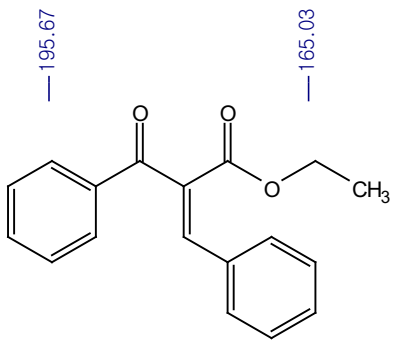
Sample : Compound 15

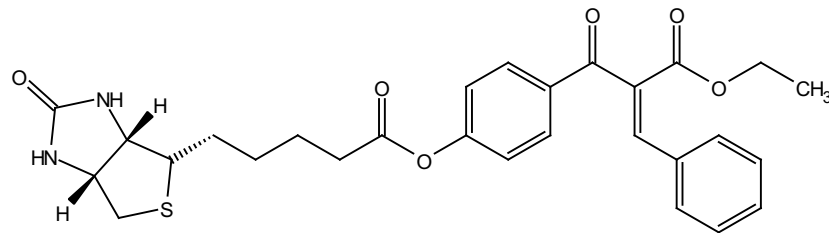
1H NMR of compound 15



^1H NMR (300 MHz, Chloroform- d) δ 8.93 (d, J = 0.9 Hz, 1H), 8.02 – 7.96 (m, 3H), 7.36 (dd, J = 7.9, 1.9 Hz, 2H), 7.30 (dd, J = 5.6, 1.3 Hz, 1H), 7.28 – 7.23 (m, 1H), 7.21 – 7.15 (m, 2H), 6.90 (s, 1H), 4.86 (dd, J = 7.5, 5.2 Hz, 1H), 4.30 (dd, J = 5.4, 2.8 Hz, 1H), 4.24 (q, J = 7.0 Hz, 2H), 3.22 (dd, J = 10.7, 5.1 Hz, 2H), 2.98 (dd, J = 13.6, 5.3 Hz, 1H), 2.61 (t, J = 7.3 Hz, 2H), 1.87 – 1.71 (m, 5H), 1.58 (q, J = 7.5 Hz, 2H), 1.21 (t, J = 7.1 Hz, 3H).







^{13}C NMR (101 MHz, Methanol- d_4) δ 194.67 (d, $J = 13.3$ Hz), 171.57, 164.95 (d, $J = 32.5$ Hz), 163.51, 155.45, 142.30, 141.50, 133.54, 133.00, 132.81, 131.74, 131.60, 131.13, 130.95, 130.51, 130.31, 130.09, 129.80, 128.55, 128.44, 127.86, 122.11, 115.30, 61.96, 61.51 – 60.73 (m), 60.23, 55.61, 39.66, 34.37 – 31.94 (m), 29.79 – 26.84 (m), 25.47 – 23.48 (m), 13.02 (d, $J = 2.4$ Hz).

